Final Technical Report

External Grant Award Number: G11AP20031

Title: Seismic Velocity and Attenuation Tomography in the Sacramento-San
                                Joaquin River Delta Area

Investigators: Clifford Thurber
                                University of Wisconsin-Madison
                                1215 W. Dayton St.
                                Madison, WI 53706
                                Phone: (608) 262-6027, FAX: (608) 262-0693
                                thurber@geology.wisc.edu

Term Covered by the Report: January 1, 2011 - December 31, 2013

Funding expended $160,000.00

Final Report

Seismic Velocity and Attenuation Tomography in the Sacramento-San Joaquin River Delta Area

External Grant award number G11AP20031

Investigator: Clifford H. Thurber
University of Wisconsin-Madison
Department of Geoscience
1215 W. Dayton St.
Madison, WI 53706
(608)-262-6027 [voice]; (608)-262-0693 [FAX], thurber@geology.wisc.edu

Report term: January 1, 2011 to December 31, 2013
Funding expended: $160,000.00

Investigations undertaken

We carried out a study of the three-dimensional (3D) seismic velocity and attenuation structure of the Sacramento-San Joaquin River Delta (SSJRD) and surrounding region in collaboration with Donna Eberhart-Phillips (consultant) and Joe Fletcher and coworkers at the USGS in Menlo Park. Our work involved incorporating new seismic data recorded by temporary USGS stations deployed within the SSJRD area into an existing dataset and (a) refining the 3D seismic velocity model of the SSJRD and surrounding region and (b) developing the first body-wave seismic attenuation model for the region. In particular, we pursued four lines of research: (1) incorporating new data from the USGS temporary stations into tomographic inversions for body-wave velocity structure; (2) carrying out joint body-wave/gravity inversion to determine seismic velocity and density structure; (3) utilizing the expanded seismic dataset for regional body-wave attenuation tomography; and (4) carrying out ambient noise tomography (ANT) to determine Vs structure. Improved knowledge of the 3D seismic velocity and attenuation structure, especially for S waves, is important for evaluating the potential for significant ground motion amplification in the SSJRD area. Our effort in Year 1 (2011) was mainly in tasks 1 and 4. Our efforts in Year 2 (2012) concentrated in tasks 2, 3, and 4. We requested and received a one-year no-cost extension to compensate for delays in obtaining data from our USGS collaborators and to provide time to produce a manuscript for publication. Our effort in Year 3 (2013) was concentrated in task 3 and in preparing a manuscript for submission to a journal in December 2013.

Accomplishments

Body-wave velocity tomography

We incorporated data from 82 earthquakes recorded by temporary USGS seismic stations in the SSJRD into a refined tomographic inversion for 3D P-wave velocity structure in the SSJRD and surrounding region (Figure 1a). We incorporated manually picked P-arrivals from YU network stations for 82 events into our dataset and included supplemental earthquake arrivals for these events from the Northern California Earthquake Data Center. Our inversion employed a grid spacing of 10 km horizontally and 3 to 10 km vertically. This result is an update of the northern California and statewide models published in Thurber et al. (2009) and Lin et al. (2010), using their datasets, model grid, and inversion parameters as the starting point. The previous models had almost no observed data within the SSJRD. Our updated model (Figure 1b) confirms the very sharp, steeply dipping velocity contrast on the western edge of the northern Delta found by Thurber et al. (2009), but with improved spatial resolution. With further new data, including records from new stations to be deployed in the northern Delta, and constraints from additional data types, our velocity model could potentially be improved further in the future.

Joint gravity-body wave velocity tomography

Following our effort in Year 1 to update the existing P-wave velocity model for the SSJRD and surrounding region, we expanded our work in Year 2 to develop and apply joint gravity-body wave velocity tomography to the region. Gravity data complement body-wave data by providing information on shallow density structure, and are particularly effective at delineating lateral variations in shallow structure. Seismic body waves provide better depth resolution but are limited by the spatial distribution of earthquake and receiver locations.

Joint inversions of body-wave arrivals and gravity data have been performed both sequentially and simultaneously. For a sequential inversion of the two data types (Lines et al., 1988), seismic arrival-time data are first inverted for velocity, which is then transformed to density using empirical relationships (Birch, 1961; Gardner et al., 1974; Christensen and Mooney, 1995; Brocher, 2005). Next, gravity data are inverted to perturb the density model, which is then converted back to a velocity model. That velocity model serves as the starting point for the next iteration of the velocity inversion, and so on to convergence. The simultaneous method is a true joint inversion where arrival-time and gravity data are inverted in the same step, with a constraint based on the empirical density-velocity relationships to link the two data sets together (Lees and VanDecar, 1991; Parsons et al., 2001; Roecker et al., 2004). Due to the rapid fall-off of gravity resolving power with distance, most joint body-wave/density inversions have been limited to local scales (Savino et al., 1977; Lees and VanDecar, 1991; Nielsen and Jacobsen, 2000; Roecker et al., 2004; Roy et al., 2005), but regional scale (Parsons et al., 2001) and even global scale (Forte et al., 1994) joint inversions have been attempted.

The USGS operated a temporary seismic network (network code YU) comprising approximately a dozen sites in the SSJRD region. The temporary network's initial deployment included 7 stations in 2006 and peaked at 11 active stations at one time during 2008 and 2009. Due to the close spacing of some stations, for our purposes the network effectively started with 4 stations and peaked at 9 stations. We incorporated manually picked P-arrivals from YU network stations for 82 events into our dataset and included supplemental earthquake arrivals for these events from the Northern California Earthquake Data Center.

Our gravity dataset comes from the NGS99 database (National Geophysical Data Center), a 1.6 million record compilation of gravity surveys taken by United States governmental organizations and academia. The NGS99 stations have been adjusted to the International Gravity Standardization Net 1971 (Morelli et al., 1971), gravity anomaly latitude corrections were calculated using the Geodetic Reference System 1967 theoretical gravity formula, and Bouguer anomalies were calculated assuming a density of 2.67 g/cm^3. There are 37,958 samples in the database that lie in the bounds of 36° N and 40° N and between 119.5° W and 123.5° W that was used in this study. The gravity data have good spatial coverage of the SSJRD and the adjacent Great Valley. We determined and removed the regional trend in the gravity data, perpendicular to the Great Valley, using a least squares fit. We then interpolated the gravity data to a regular grid with 32 nodes per side, spaced 8 km apart and centered at the origin of our Cartesian model space. After interpolation we upward continued the data to a height of 5 km (Blakely, 1995).

Our seismic-gravity joint tomographic inversion algorithm (tomoDDG) is based on the double-difference tomography algorithm tomoFADD (Zhang and Thurber, 2006), which is regional in scale, performs finite-difference travel time and ray path calculations, and allows flexible node spacing. We updated the tomoFADD algorithm to solve simultaneously for slowness from arrival time residuals and Bouguer gravity anomalies, using an empirical relationship to convert density perturbations to slowness. We use the Talwani equations for a rectangular parallelepiped volume (Talwani, 1973) to calculate the forward problem for determining Bouguer gravity anomaly residuals. We use the equation of Brocher (2005) to construct our joint relationship between P-wave slowness (reciprocal of velocity) and density, a 5th degree polynomial. The joint inversion then solves the system of equations

$$\begin{bmatrix} G_e & G_r \\ 0 & wG_g \end{bmatrix} \begin{bmatrix} \Delta x \\ \Delta u \end{bmatrix} = \begin{bmatrix} \Delta tt \\ w\Delta g \end{bmatrix}$$

where matrix G_e is the earthquake location kernel, matrix G_r is the ray-path kernel, vector Δx contains the perturbations to earthquake location and origin time, vector Δu contains the perturbations to slowness, vector Δtt contains the arrival time residuals, 0 is a matrix of zeros, w is a weighting factor applied to the gravity portion of the problem, G_g is the modified gravity kernel, and Δg is the gravity residual. The gravity kernel that quantifies each model cell's contribution to all the gravity anomaly values is constructed using the Talwani equations and the empirical density-P-wave velocity relationship of Brocher (2005), parameterized as a 5th order polynomial. The modified gravity kernel is the gravity kernel multiplied by a velocity-dependent factor to transform density perturbations to slowness perturbations. The nonlinear slowness-density relationship presented some difficulties in the inversion process by causing overshooting of model perturbations. This problem was overcome by limiting the perturbation step size at each iteration, a common practice in nonlinear inversions.

Our joint body-wave/gravity inversion is a complex, nonlinear problem that involves a trade-off between fitting the two datasets wherever they are inconsistent with one another and where our assumed empirical relationship between density and velocity is not a perfect match for the actual density-velocity relationship of the earth. Our starting velocity model was a converged solution of seismic-only tomography. After the first iteration we saw a 9% percent increase in misfit to the arrival-time residuals as the velocity model is first perturbed trying to fit gravity residuals. For the later iterations we then saw a consistent decrease in arrival-time residuals until the final residual was 2% greater than the initial seismic-only residual. The fit to the gravity data improved after each iteration, ending with a 19% improvement in fit. An example cross-section of key velocity contours through the SSJRD from the joint inversion model compared to the previous results is shown in Figure 2a. Map-view slices through the 3D model are shown in Figure 2b.

Figure 3 shows a 3D view from the south of the 5.5 km/s iso-surface, representative of the basement interface at depth. We see a northwest-southeast trending deep zone corresponding to the western edge of the Great Valley sedimentary basin. Beneath the southeast portion of the SSJRD a plateau in the basement is evident with a sharp drop off to the southwest (visible as a gray shadowed area). The deeper basement depths wrap around the plateau to the west and north. Our seismic velocity model suggests the SSJRD may be prone to basin amplification of seismic waves, basin-induced surface waves, and focusing effects.

Ambient noise tomography

We cross-correlated and stacked hour-long signals of ambient seismic noise between pairs of seismic stations to compute Green's functions simulating the Earth response between seismic stations, predominantly in the form of Rayleigh waves. Prior to correlation, we bandpass-filtered the continuous waveforms and performed automatic gain control and spectral whitening as described in Masterlark et al. (2010). An example is shown in Figure 4a. We then produced "energy diagrams" from our waveform correlations by applying narrow frequency band filters over a range of center frequencies to the data, yielding amplitude versus time at a given frequency. Since the station separation distance is known, the time axis can be transformed into velocity. Plotting these (normalized) amplitudes as a function of velocity and frequency produces the "energy diagrams," and picking the maximum amplitude at each frequency provides the group velocity dispersion curve. An example is shown in Figure 4b.

We found that utilizing multi-component cross-correlations, rather than just the standard vertical-vertical cross-correlations, was critical for producing higher-quality Green's functions. In particular, using the vertical-radial correlations is an effective way to enhance the Green's function extraction, especially for the case of non-uniform noise distribution. An example is shown in Figure 5. We also tested the assumption that, for example, the radial-radial and transverse-transverse Green's function can be obtained by processing the original NS and EW horizontal component data and then rotating those components to radial and transverse, as opposed to rotating the raw data before processing to extract the Green's function. Our tests indicate that this process-then-rotate approach is adequate within typical noise (Figure 6). We then assembled a suite of Green's functions for many station pairs in and around the SSJRD (Figure 7). Our empirical Green's functions are in good agreement with published cross-correlations and match earthquake waveforms sharing similar paths.

This was followed by tomographic inversion using the procedure described in Masterlark et al. (2010). Our tomography grid had its coordinate origin at latitude 37.7787° and longitude -121.2782° with

4

the Y axis oriented north. The cell size was 10 km in the horizontal direction and 1 km in the vertical direction, with maximal extents of X=-220 and 220 km, Y = -320 and 280 km, and Z = 0 and -50 km. Group velocity maps were created from our cross-correlations for each frequency from 0.04 to 0.448 Hz (~ 2 to 25 s periods) at 0.003 Hz intervals. We only accepted paths that were at least one wavelength long, had a signal to noise ratio of at least 7 and had group velocities between 0.5 and 5 km/s. We then used surface-wave inversion to derive a 3D shear wave velocity model for the SSJRD and surrounding area. Our group velocity and shear velocity maps are in good agreement with published regional scale models, but are resolved at a finer scale. We also performed a checkerboard test for group velocity resolution at 0.15 Hz. From our inversion results (Figure 8), we found that the maximum depth of the basin beneath the SSJRD is approximately 15 km, with the Great Valley ophiolite body rising to 10 km below the surface east of the SSJRD.

Our seismic velocity model suggests the SSJRD may be prone to basin amplification of seismic waves, basin-induced surface waves, and focusing effects. Olsen (2000) estimated the site response for the Los Angeles basin using 3D finite-difference, finite-fault simulations which reproduced the particle velocities from the 1994 Northridge earthquake reasonably well. The Olsen (2000) study found the greatest basin amplifications corresponded to the deepest portions of the basin with amplification factors around 6 for 9 km basin depth. Furthermore the greatest amplifications seemed to be at locations further from the basin edge. These findings indicate that the northwestern portion of the SSJRD could experience large ground motion amplifications.

The SSJRD may also experience focusing effects due to the irregular basement topography in the southeast portion of the SSJRD. Semblat et al., (2002) performed simulations of wave amplifications for a flat-bottomed and an irregularly shaped basin and found the irregular basin shape led to focusing effects. Hartzell et al. (1996) attribute amplifications at the southern edge of the San Fernando Valley to irregular layer boundaries. This suggests there is a possibility the "plateau" in the basement topography for the SSJRD could potentially focus seismic waves.

Body wave attenuation tomography

The SSJRD region, at the middle of the Great Valley, is a very low elevation area at the confluence of the major rivers as the water flows out to the San Francisco (SF) Bay (SFB). This 3000 km^2 region forms the largest estuary on the west coast of North America. It contains a system of levees that may be prone to failure from a major earthquake in the SF Bay Area or on faults along the western border of the Great Valley, and multiple failures of the levee infrastructure could have a catastrophic effect on the California water supply system (Lund et al., 2007; URS/JBA, 2009). The largest magnitude earthquake source may occur on faults over 50 km away from the SSJRD. Thus regional attenuation is important to consider for evaluating the potential for strong ground motion. Variations in the 3D Q structure have been found to have a significant influence on attenuation rate in other regions (Eberhart-Phillips et al., 2010).

The Great Valley basin shape is asymmetric with shallow dipping basement on the east, and the western margin disrupted with tectonic wedging against the Coast Ranges; basin depth may be greater than 10 km (Wentworth et al., 1995; Thurber et al., 2009). The basement is composed of Great Valley Ophiolite oceanic crust and Sierra Nevada Batholith, as described by Godfrey and Klemperer (1998). The mafic rock of oceanic crust would be expected to have very high Q in contrast to the sedimentary rock, and this could have an additional influence on the propagation and attenuation of seismic energy. Strong underlying oceanic crust may have had a significant effect in the energetic earthquake sequence in Canterbury, New Zealand (Reyners et al., 2013). In this study we aim to determine the 3D Qp and Qs properties of the SSJRD region to provide a useful 3D Q model for other seismic analyses.

Seismic properties of the levees and the SSJRD have been studied by Fletcher and Boatwright (2013). They installed stations on levees and farmland (Figure 9). The site responses for the levees show large resonance at 1-3 Hz with amplitude of 10-15. They also observed basin waves generated at the edge of the low Vs basin, and determined that the upper 2 km has Vs of 0.3-1.1 km/s, due to weak peat, eolian, and fluvial sediments. The availability of data from their temporary array motivates our analysis of Q structure.

There have been several regional seismic velocity studies of the area but little work on attenuation. The 3D seismic velocity structure of northern California region from local earthquake tomography was

determined by Thurber et al. (2009). Lin et al. (2010) determined a comprehensive 3D velocity model for the state of California, starting with a coarse model and a-priori Moho to have a reasonable model even in areas of sparse data coverage. Active source seismic profiles have been completed to the north and south of the Delta region (Wentworth and Zoback, 1987; Godfrey et al., 1997), and together with potential field studies have been summarized by Godfrey and Klemperer (1998). The seismically active SF Bay Area has been studied in more detail including 3D models (Hole et al., 2000; Thurber et al., 2007; Hardebeck et al., 2007), and active-source profiles (Holbrook et al., 1996), which found seismic properties change substantially across the fault zones. Malagnini et al. (2007) determined a uniform frequency-dependent attenuation relation for the Bay Area of $Q(f)=180\,f^{0.42}$, through an empirical fit to peak amplitudes obtained at discrete frequencies. For estimating long-period ground motion for large earthquakes in the Bay Area, Aagaard et al. (2010) developed rupture models, using a geologically based 3D velocity model and a frequency-independent Qs (Vs) relation based on modeling of the Northridge earthquake (Brocher, 2008).

Attenuation is inversely proportional to Q so that high attenuation is indicated by low Q. Intrinsic attenuation and scattering attenuation contribute roughly equally to crustal attenuation (Frankel, 1991). As summarized by Winkler and Murphy (1995), intrinsic attenuation is primarily the result of viscous damping from local pore fluid motion and grain boundary effects, and thus is highly dependent on permeability, which allows energy-absorbing fluid motion. Attenuation increases as permeability increases, but the relevant permeability need not be capable of supporting regional fluid flow. Increased fluid pressure or increased fluid viscosity will also increase attenuation. Scattering attenuation results from the redistribution of seismic energy as it passes through heterogeneous rock, and incorporates velocity fluctuations of much larger dimension than grain size, up to the sampled wavelengths of 0.3-3 km. (Frankel, 1991). Our method cannot separate scattering and intrinsic attenuation, and the results cannot be directly related to laboratory-measured intrinsic attenuation values. In the ductile part of the crust, attenuation occurs by grain-boundary sliding, and this is influenced by grain-size, as well as temperature, water and mineral content (Jackson et al., 2002), and hence grain size reduction in shear zones will greatly decrease Q. Below the crust, at temperatures over 900°C, temperature becomes the primary controlling factor in attenuation, as the deformation behavior changes from elastic to anelastic to viscous (Jackson et al., 2002).

We selected earthquakes that were recorded on the Delta array of Fletcher and Boatwright (2013), as well as other earthquakes that sample the study area. Waveform data were obtained from the Northern California Earthquake Data Center (NCEDC), which includes broadband and short-period data from the U. S. Geological Survey (USGS), Univ. California Berkeley (UCB) and EarthScope. The large Sierra Nevada EarthScope Project broadband array operated May 2005-September 2007 and has been used to determine along-strike variations in lithosphere properties, with the thickest root remaining in the central Sierra Nevada on the northwestern side of our study area (Frassetto et al., 2011). We selected 124 spatially distributed earthquakes to sample the region, with magnitude 2.2-5.6, during the period 2005-2011, with 34 during the temporary Delta deployment. Figure 10 shows the stations and earthquakes that were used. We included both vertical and horizontal components. Catalog arrival times for the NCEDC data were used and Delta array arrival times were hand-timed (Teel, 2012). Hypocenters were obtained from the double-difference catalog (Waldhauser, 2009; http:/ddrt.ldeo.columbia.edu/DDRT).

Q describes attenuation where 1/Q is the fractional loss of energy per cycle, so high Q indicates low attenuation and low Q indicates high attenuation. For constant Q and seismic velocity (V),

$$A(x,f) = A_0 \exp -(\pi f/QV)x \qquad (1)$$

where A is amplitude, x is propagation distance, f is frequency and A_0 is initial amplitude. Q may exhibit frequency dependence with exponent α, often expressed as

$$Q(f) = Q_{f0}(f/f_0)^\alpha \qquad (2)$$

where f_0 is a reference frequency, which is 10 Hz in this study.

The parameter t* describes the whole path attenuation:

$$t^* = x/(QV) \tag{3}$$

When Q and V vary spatially, t* is related to Q by

$$t^* = (f/f_0)^{-\alpha} \int_{ray} ds /[Q_{f0}(s)*V(s)] + t^*_{station} \tag{4}$$

Hence t* data from local earthquakes are amenable to inversion for 3D Q, where $t^*_{station}$ are station terms that can be included in the inversion.

The velocity amplitude spectra are used to obtain the t* data:

$$A_{ij}(f) = 2\pi f \, \Omega_0 \frac{f_c^2}{\left(f_c^2 + f^2\right)} \, \exp[-\pi f \, (t^*_{ij})] \, T_j(f) \tag{5}$$

The observed spectra $A_{ij}(f)$, for the event i at the station j, is fit with three parameters: the low-frequency spectral level, Ω_0, which is proportional to seismic moment and here incorporates the frequency independent geometrical spreading; the corner frequency, f_c, and t*, assuming an ω^{-2} source model. A site response $T_j(f)$ can be used. We include the frequency-dependent term when fitting the spectra and so determine frequency-dependent t* data, with which Q_{f0} can be obtained.

For a given f_c, each velocity spectrum is fit by nonlinear least-squares for Ω_0, and t*(Wang et at., 2009), using the portion of the 1-32 Hz frequency band that has signal-to-noise ratio (S/N) over 1.25. The best-fitting corner frequency, f_c, of the event is estimated by a grid search using all of the recordings for each event. The search range of f_c is based on values approximated for 1-60 MPa stress drop, using a circular fault (Madariaga, 1976; Abercrombie, 1995). In order to weight each t* residual in the Q inversion, we estimate a quality for the t* observation based on how well the spectrum is modeled, the range of frequency that is modeled, and the proportion of the range that has S/N > 2.3. For this study, we consider frequency dependence in Q but do not vary the frequency dependence throughout the 3D model, so the frequency dependence is included in the t* fitting (Figure 11).

The site response, $T_j(f)$, incorporates local effects that are common to all the earthquakes at a station. First t* are obtained without site response. Then site response is determined by averaging together all the residuals for each station, using a 5-point moving average and limiting the effect of high residuals and cases where there are few good signal-to-noise ratio (S/N) observations. The site response correction has little effect on the t* values and no systematic effect, since it is calculated from the residuals and can be negative as well as positive. Removal of site response improves the misfit, such that about 5% more data have usable t* values. The quality parameter combines the S/N and misfit, and for values greater than 2, the t* are not used in the inversion. Thus in the top row of Figure 11, SRT has a misfit of 1.7 and is barely usable, and STF and BJOB have corrected spectra (heavy lines) that provide allowable misfits of 0.8 and 0.4.

For P data, t* estimates are obtained from a 2.5 s window starting at the P arrival. An alternate method is used for S wave data, since there are fewer clear S arrivals and they are biased to representing higher Q paths. Useful S t* estimates have been selected within a -2 to 16 s window around a predicted S arrival, using the 5-95% energy integral, and using a noise window 3-0.5 s prior to the P arrival to compute S/N. Spectra are fit over the frequency range that has S/N over 1.25, and clipped data are removed. There were 8,538 P t* data, and 10,659 S t* data. The S used both horizontal and vertical component data.

Other types of studies have favored frequency dependence, with many studies providing exponents in the range of 0.4 to 0.6. Boatwright and Seekins (2011) considered data to low frequencies of 0.2 Hz for eastern North America and determined $\alpha = 0.5$. For southern California, Raoof et al. (1999) determined $\alpha = 0.45$ and Boatwright et al. (2002) determined $\alpha = 0.6$. For northern California, Malagnini et al. (2007) determined $\alpha = 0.42$. Our preliminary analyses of a wide range of α showed that most spectra have equivalent fit with or without frequency dependence, and a small proportion favor either $\alpha = 0$ or $\alpha = 0.4$-

0.6. The exponent of 0.5 is consistent with most other crustal studies, and thus we will carry on with that value for our frequency-dependent Q analyses. An example of t* fitting for the S spectra is shown in Figure 11, comparing the results for frequency independent (red line) and frequency dependent for $\alpha = 0.5$ (green). In each plot, the frequency independent is the most bent line. The t* fits for all the data are compared in Figure 12d-e. Considering a significant reduction in misfit of ≥ 3, for P spectra, 2% have improved fit for $\alpha = 0.5$ and < 1% for $\alpha = 0$. For S spectra, 11% have improved fit for frequency dependence and 1% for none. Given this improved fit and the other California studies, we compute frequency-dependent Q in this work. In general, frequency dependence remains an uncertain issue. The ray-path based Q obtained from t* is a useful parameter for earthquakes studies yet it encompasses a varied range of intrinsic and scattering attenuation aspects. Comparing all our t* data for $\alpha = 0$ to those for $\alpha=5$, there is a strong linear relation with $t^*_{\alpha 5} \sim 1.8 \, t^*_{\alpha 0}$ (Figure 12a-b). Hence 3D Q models would have similar patterns for $\alpha = 0$ and $\alpha = 5$. Considering the frequency dependent 3D models computed in this study, frequency independent $Q_{\alpha 0}$ would be ~1.8 $Q_{f10\alpha 5}$.

Comparing the t* for S and P for the same paths (same event and station), there is not a distinct linear relationship (Figure 12c). This implies that the Qs/Qp relation probably varies for different materials and locations. Lines for slopes of 1.2 and 1.0 are shown. For the latter, a constant factor (0.015 on the y intercept) is positive and suggests a uniform low Qs feature that affects all the t*. There may be shallow low Q material, which would be sampled by all paths, which is especially low in Qs compared to Qp. Note that our S window includes more scattering and we cannot necessarily infer a general relation for intrinsic attenuation.

The t* data were used in inversions for 3D Qp and Qs (Rietbrock, 2001; Eberhart-Phillips and Chadwick, 2002) with ray paths determined from the 3D velocity model already derived. The solution is obtained by iterative damped least squares, with the damping parameter for each inversion chosen empirically by evaluating a trade-off curve of data variance and solution variance. We excluded unrealistic negative t* data. The recent inversion code that we used incorporates receiver-differential t* values along portions of ray paths near stations, which provide more detailed resolution on the receiver side (Eberhart-Phillips and Reyners, 2012). Overall, the S t* data had higher residuals than the P t* data, which may relate to the S data representing more scattering that the P data. Our procedure was to first obtain a regional initial model, then compute a 3D model for the study area, and finally to run additional iterations for the surface layer. We included station t* terms for stations outside of the study area.

Well-constrained regional 3D velocity models have already been developed (Figure 13a-b; Lin et al., 2010). Thus to establish the regional 3D Q initial model, we solved for Q as a function of V, using a relatively small number of regional events (108). In general, Q is not a function of velocity, and it often displays significant variations due to temperature and fluid content even when the velocity is relatively uniform. However, broadly different types of material will also differ in Q. The extensive sedimentary deposits will have low Q relative to competent rock, and metamorphosed mafic rock may display relatively high Q. In this initial stage, Q was parameterized at 10 defined V values, with linear interpolation between those values. Seismic rays from the regional earthquakes were traced through the 3D velocity model of California of Lin et al. (2010), and the partial derivatives were accumulated for Q(V), based on the V at each ray path point. The resulting Qp function has low Qp (< 200) for the low Vp rock (< 5 km/s), rising to 500-600 for rock with moderate Vp (6-7 km/s) (Figure 14). High Qp (> 900) is found for the high velocity uppermost mantle (Vp > 8 km/s), although Qp decreases for higher velocity (> 8.7 km/s) as the mantle becomes warmer and more ductile at greater depth. The regional 3D Qs initial model is illustrated for 4 km and 27 km depth in Figure 13c-d. The low Q Great Valley is apparent in the shallow plot, and in the deeper plot, the high Q uppermost mantle is apparent, with crustal thickening under the Sierra Nevada.

The regional 3D Qp initial model achieved a 44% reduction in data variance from the 1D model variance, and the 3D inversion Qp model achieved a further 27% reduction relative to the 1D result, giving a total 71% reduction in data variance. For Qs, the regional model achieved 42% reduction and the 3D model achieved 31% reduction, for a total 73% reduction in data variance.

The final 3D models are shown for Qp in Figure 15 and for Qs in Figure 16. The resolution is shown in Figure 17 with the spread function (Michelini and McEvilly, 1991). Where the spread function (SF) is low (dark gray), the resolution is best, with little smearing. In areas with moderately high SF (> 3), the Q

pattern is reasonable, but the shape of features and specific Q values are weakly constrained, and there may be additional detail that has not been imaged. For SF > 3.5, there is little resolution and only coarse broad features may be imaged with poor definition of their shape or extent. The Q plots have magenta lines for the SF = 3.5 contours. The SF contours show that the resolution is best in the southwestern half of the study area where there are more earthquakes and stations. The patterns of Qp and Qs resolution are similar, but the Qs model has slightly more data. Little information is obtained in much of the upper 8 km of the Sacramento and San Joaquin basins, which shows the importance of obtaining the regional initial Q model. For comparison, we also completed a Qp inversion with a 1-D initial model. Notably, it does not fit the data as well (11% poorer fit), and it exhibits vertical smearing of the shallow low Q features.

The Q results show very low Q in the upper few km of the SSJRD, and a few other areas such as the Hayward-Calaveras fault junction. Moderately low Q is found in the upper 10 km in the Delta region, the Sacramento basin, and along the faults in the eastern North Bay Area. In contrast, moderately high Q is found south of the SSJRD, implying potentially stronger ground motion for earthquake sources to the south. There is a strong Q contrast at the base of the crust, with underlying very high Q. This implies that earthquakes ~100 km away may still have potential for significant strong ground motion.

Great Valley Basin

The Sacramento and San Joaquin Basins consist of Great Valley Sequence (GVS) sedimentary rocks overlying crystalline basement of obducted oceanic plate, the Great Valley ophiolite, or Sierra Nevada batholith (Godfrey and Klemperer, 1998). Wentworth et al. (1995) fit the basement surface from numerous wells and several seismic refraction and reflection profiles. Qp and Qs in the Great Valley are < 50 at shallow depth (Z = 1), where there is good resolution, and near 100 at 4-8 km depth (Figures 15a-b, 16a-b). There is a strong contrast to basement Qp and Qs of ~350-500, with Great Valley ophiolite having greater Q than Sierra Nevada batholith, and Qs being greater than Qp.

Along the eastern margin, the basin shape in Q is similar to the mapped basement, as illustrated by the -4 km basement contour of Wentworth et al. (1995) plotted on the 4 km depth map views (Figures 15b, 16b). The imaged low Q basin is broader and deeper in the north (Y > 225 km, Z = 8 km) and is deepest in the western SSJRD (Z = 14 km), consistent with the Vp model of Thurber et al. (2009). At shallow depth, the lowest Q areas (< 25) occur in the SSJRD, northwest of Stockton and northeast of Mt. Diablo. Given the patchy resolution at 1 km depth, we cannot discern whether or not these areas represent a broader zone of very low Q. The low Q is consistent with thicker alluvium and permeable relatively high porosity sedimentary rock.

Great Valley Ophiolite

The Great Valley ophiolite (GVO) is a block of backarc oceanic plate that collided with and obducted up on the continent, and is thicker in the north under the Sacramento basin, where it includes both oceanic crust and mantle (Godfrey and Klemperer, 1998). We image this mafic rock with high Q under the Great Valley, with slightly higher Qs than Qp (Figure 18a). There appears to be a change in structure at the southern end of the Pittsburgh-Kirby Hills fault, as seen in the 14-20 km depth map plots (y = 230, x = 30 to 50; Figures 15d-e, 16d-e). The high Q GVO feature steps eastward and is less pronounced. To the north there is a substantial block of high Q (Qs > 700) at 20 km depth under the Sacramento basin. This would represent the GVO oceanic mantle section, as determined by Godfrey et al. (1997) on a profile 100 km further north. This large coherent block of oceanic crust and mantle forms a strong competent region under the basin. The sharp contrast in properties above emplaced oceanic crust is similar to that observed in Canterbury, New Zealand, where strong basement was related to the energetic earthquake sequence (Reyners et al., 2013). The deepest part of the low Q basin is near the southern end of the thick block at the transition to the thinner GVO of the northern San Joaquin basin, which contains solely oceanic crust (Godfrey and Klemperer, 1998).

Franciscan Wedge

The Franciscan terrane formed in a long-lived accretionary prism and contains a primarily graywacke melange including mafic volcanics and ophiolites, with increasing metamorphic grade toward the east (Blake et al., 1988). During collision with the continent, extensive tectonic wedging occurred along the

9

western Great Valley, resulting in imbrication of Franciscan and GVS rock, and packets of mantle ophiolite along the Coast Range margin (Godfrey et al., 1997; Moores et al., 2002). Thus GVS rock extends under Franciscan below the Diablo Range and northern Coast Range as shown by Wentworth et al.'s (1995) contours. The contoured basement surface is drawn on the Q cross-section near their CC refraction profile (Figure 18c-d). The steep dip of the basement on the southwest to 14 km depth is consistent with a deep low Q zone.

A more vertical edge to the very thickest GVS section is seen on the Y = 240 km section (Figure 18b) near the Pittsburgh-Kirby Hills fault (PKHF). Based on a more detailed velocity model, the PKHF has been inferred to be a steeply northeast dipping fault, which may be associated with an uplifted fragment of ophiolite (Thurber et al., 2009). This would imply that the Suisun Bay region is one area that does not have GVS thrust under Franciscan.

To the north and south, relatively horizontal ophiolite fragments are inferred to have imbricated into the wedge based on aerofoil-shaped magnetic bodies near 5 km depth (Jachens et al., 1995). The high Q features at 4 km depth under the eastern Diablo Range are consistent with such mafic ophiolite fragments ('mb' in Figure 18a, d).

Bay Area Block

In their seismic profile across the northern Coast Range, Godfrey et al. (1997) find that, west of the marginal zone of tectonic wedging, the Franciscan terrane is underlain by a coherent slab of mafic material that may be underplated basalt or stalled subducted oceanic crust. The Franciscan in the San Francisco Bay area is disrupted by the strike-slip fault systems, with a relatively narrow block of coastal Franciscan east of the San Andreas fault. There Holbrook et al. (1996) also find a mafic lower crust that may be underplated oceanic crust from ~15-25 km depth. Its reflectivity led them to infer that it has undergone extensive shear deformation.

The 3D Q results find moderately high Q (300-600) for the Bay Area block in the 4-14 km depth range, as seen in map view and cross-section (Figures 15c-d, 18b-c). This block between the San Andreas and Hayward faults lacks seismicity and the moderately high Q is consistent with a strong unit having relatively low fracture density. The seismic velocity from earthquake tomography (Thurber et al., 2009) is similar to the active source study, with up to ~6 km/s from 5-15 km depth, reaching 7 km/s at 20 km, with 8 km/s Moho at 25-30 km. The Q results for the lower crust are markedly different from the velocity. Rather than seeing high Q as would be expected for mafic oceanic crust, a low Q zone is observed under the Bay Area block at 20 km depth.

The low Q in the mafic lower crust must result from a mechanism that increased attenuation without affecting velocity. Holbrook et al. (1996) infer that this highly reflective lower crust has a diabase rheology that deforms with semi-brittle and plastic flow, and suggest that the entire lowermost crust between the San Andreas and Hayward faults serves as a zone of distributed shear. The mylonite shear zones would produce the seismic reflectivity. In ductile crust, attenuation occurs by grain-boundary sliding, and this is greatly influenced by grain-size, such that Q is roughly proportional to $d^{1/4}$, where d is grain size (Jackson et al., 2002). In high stress and low temperature regions, increased strain rate produces grain-size reduction through strain energy driven grain-boundary migration (Platt and Behr, 2011), and thus high strain zones in the ductile crust would exhibit low Q. Hence the observed low Q supports the hypothesis that the Bay Area lower crust is a broad shear zone.

Fault Zones

Very low Q values are shown in the upper few km in many places along the major fault zones (Figures 15a, 16a). This is most apparent along the Calaveras-Hayward-Rodgers Creek (CHRC) fault zone, and may relate to a combination of highly fractured material from microseismic activity and basin sediments in the fault zones. Notably, the lowest Q is observed in the basin between the Calaveras and Greenville faults, south of Mt. Diablo, where Qs < 10 at 4 km depth.

The CHRC fault zone generally is imaged as a low Q feature throughout the brittle crust (Figure 18). It has abundant microearthquakes, which would serve to maintain connected microfractures. This would reduce Q because intrinsic attenuation is largely the result of viscous damping from local pore fluid motion, and is highly dependent on permeability (Winkler and Murphy, 1995). Seismic micro-fracture

zones will produce greater fracture connectivity, whereas locked healed fault regions will have little fracture connectivity. Additionally, scattering attenuation may occur across fracture networks. Low Q or high attenuation and scattering have been observed in fault and fracture region in other areas. In the region of the Mw 7.3 western Tottori earthquake, Asano and Hasegawa (2004) found a prominent S scattering zone along and around the fault zone to 20 km depth. In this region there are zones of lineaments but no major mapped fault and the scattering was attributed to fluid-filled cracks and heterogeneous structure. In the region of the Mw 6.9 Kobe earthquake, Rietbrock (2001) found a zone of low Qp at 6 km depth where there was a high density of fault lineations and inferred partially saturated cracks, whereas most of the fault zone had moderate Qp. In the region of the North Anatolian fault zone (NAFZ), Koulakov et al. (2010) found the lowest Q at 5 km depth in sedimentary basins, and low Q at 10-20 km depth generally correlated with fracturing zones of the NAFZ, which had large earthquakes in the 20th century.

The brittle-ductile transition (BDT) can be approximated from the base of the seismogenic zone at approximately 12 km depth. In the ductile lower crust, low Q is shown beneath the San Andreas and CHRC faults. The San Andreas, which has large cumulative strain but low microearthquake activity, has the most distinctive low, of Qs < 100. This would represent an extensively sheared zone of grain-size reduction, which is likely to be at least several km wide in order to be imaged on our coarse grid. Such shear zones are included in some deformation models to allow viscoelastic behavior and to improve the geodetic fit over the course of a seismic cycle. For the San Andreas and CHRC system, Kenner and Segall (2003) found that optimal models contain discrete shear zones ~5 km wide with short relaxation times, plus a structure with a long relaxation time which may be a distributed shear zone in the lower crust and/or upper mantle. The 3D Q results are similar to the optimal viscoelastic rheological model, suggesting that 3D Q models may aid the development of viscoelastic numerical models.

Summary of Q results

We computed 3D Qp and Qs models for a 220-by-220 km region around the SSJRD, using path attenuation t* values obtained for P and S data, with a longer variable window for S based on the energy integral. We used frequency dependence of 0.5 consistent with other studies, and weakly favored by the t* S data. A regional initial model was obtained by solving for Q as a function of velocity giving low Q for basins and high Q for the uppermost mantle.

In our final model, moderately low Q is found for basement rocks west of the Delta region in the eastern North Bay Area. In contrast, moderately high Q is found south of the Delta, implying potentially stronger ground motion for earthquake sources to the south. There is a strong Q contrast at the base of the crust, with underlying very high Q. This implies that earthquakes ~100 km away may still have potential for significant strong ground motion in the Delta area.

The Great Valley basin has low Q (~100) at 4-8 km depth, and the shape of the low Q basin is similar to that inferred from seismic profiles and wells. The lowest Q areas (< 25) occur in the SSJ Delta and may represent a broad zone of very low Q thick alluvium and permeable high porosity sedimentary rock.

The Great Valley ophiolite is imaged as high Q basement, with slightly higher Qs than Qp, and patterns are consistent with previous tectonic 2D profiles. The northern thicker crust-mantle block of GVO under the Sacramento basin has Q > 700, with a structural change across the Suisun Bay to the southern oceanic-crust block of GVO. There, an inferred uplifted fragment of ophiolite appears to bound the deepest part (> 10 km) of the basin.

The Bay Area block between the San Andreas and Hayward faults has moderately high Q in the brittle crust consistent with a strong unit with low fracture density. Very low Q values are found along parts of the major fault zones, notably the Calaveras-Hayward-Rodgers Creek (CHRC) fault zone which has background seismicity, and may relate to highly fractured material and basin sediments in the fault zones. In contrast, locked healed fault zones have little fracture connectivity and thus higher Q.

The ductile lower crust shows low Q zones that may be related to shear zones that have experienced grain size reduction. Low Q in the lower crust of the Bay Area block is consistent with previous interpretation of a broad shear zone between the major faults based on highly reflective lower crust. The ductile lower crust of the San Andreas and CHRC fault zones also exhibits low Q, being most distinctive under the San Andreas, which has the most cumulative strain.
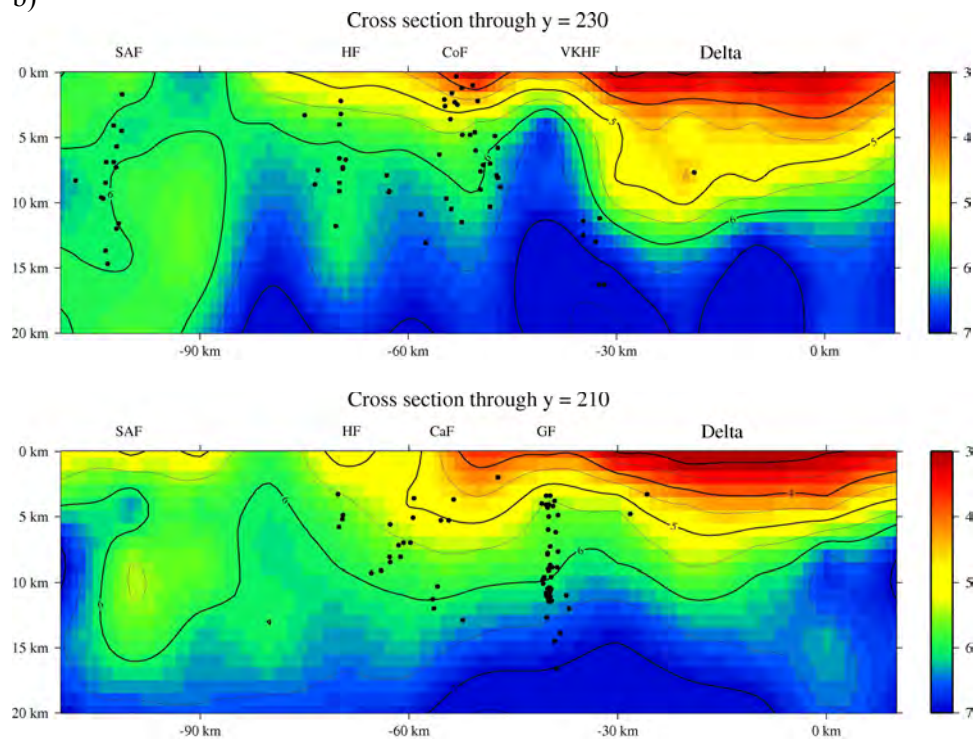
a)
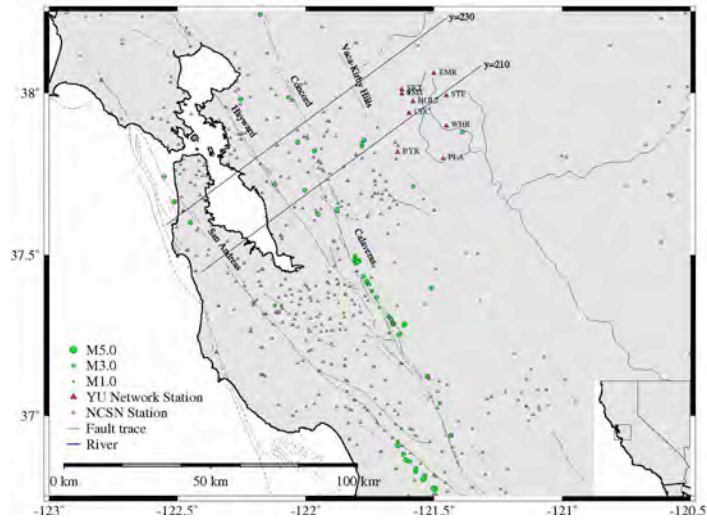
b)

Figure 1. (a) Map of earthquakes (green circles) large enough to provide usable data at the temporary SSJRD stations (red triangles). Also shown are permanent network stations (unfilled triangles), main faults (thin black lines) and rivers (blue lines). (b) Cross-sections through the 3D model as indicated in (a), showing the very strong, steeply dipping velocity contrast beneath the southwest edge of the northern Delta (y = 230 km, top) and a gentler contrast through the central Delta (y = 210 km, bottom).

a)

4 km depth

8 km depth

14 km depth

20 km depth

Vp (km/s)

b)
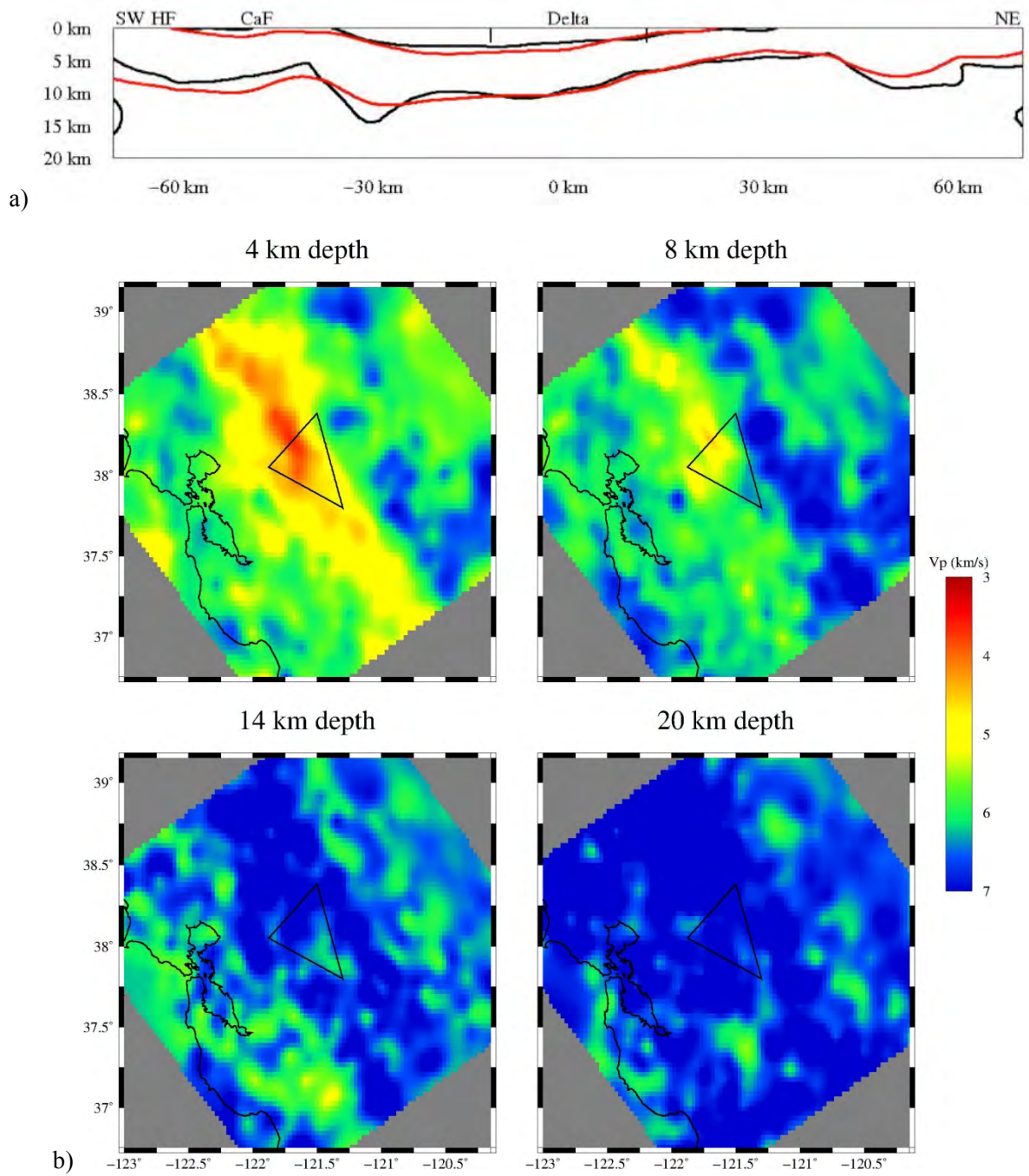
Figure 2. (a) Example NE-SW cross-section from the joint inversion model through the SSJRD. Red contours represent the seismic-only model and black contours represent the joint model. The top and bottom contours are for 4 km/s and 6 km/s, respectively. Note the deepening beneath the western Delta. (b) Map view of the velocity model at 4, 8, 14, and 20 km depth. Velocity values are shaded from 3km/s (red) to 7 km/s (blue). Black triangle outlines general area of the SSJRD.
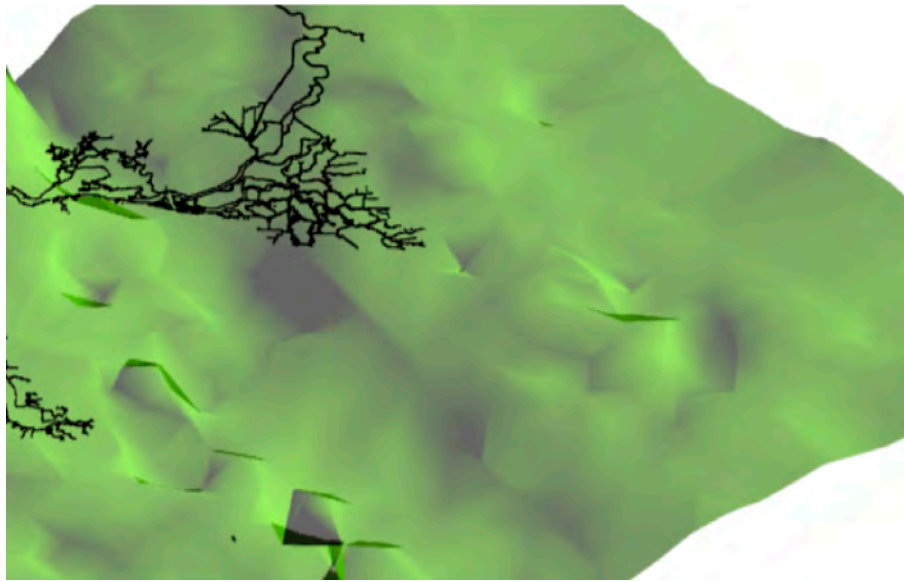
Figure 3. Perspective view of the 5.5 km/s iso-surface, seen from the south. Note the deeper area of low velocities near the western edge of the Delta.
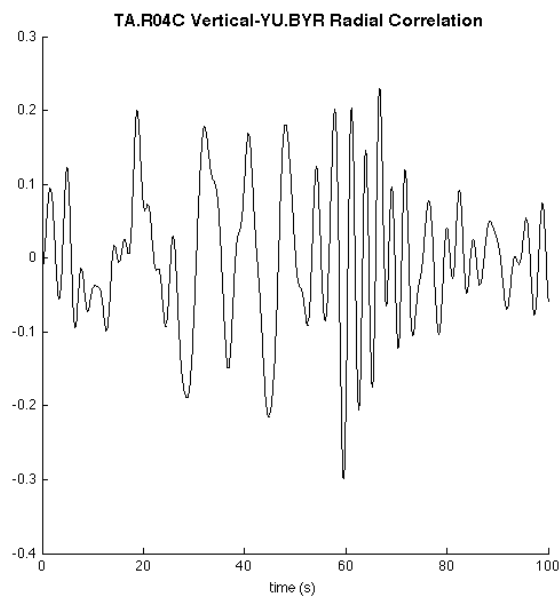
a)
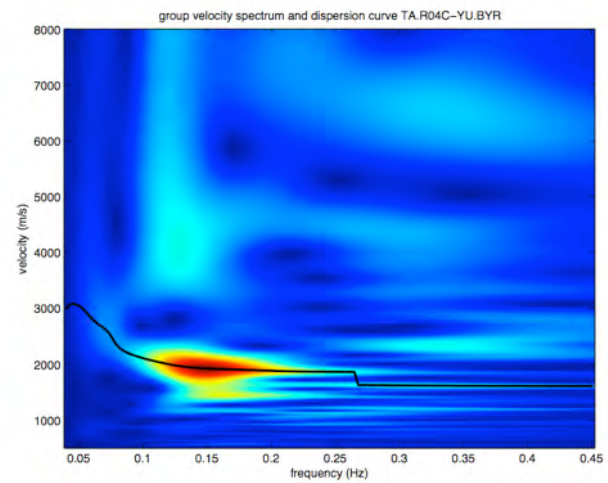
b)

Figure 4. (a) Recovered Green's function (one-sided) and (b) energy diagram for station pair R04C (vertical) and BYR (radial).

two−sided cross−correlation TA.BNLO Vertical−TA.R04C Vertical

two−sided cross−correlation TA.BNLO Radial−TA.R04C Vertical
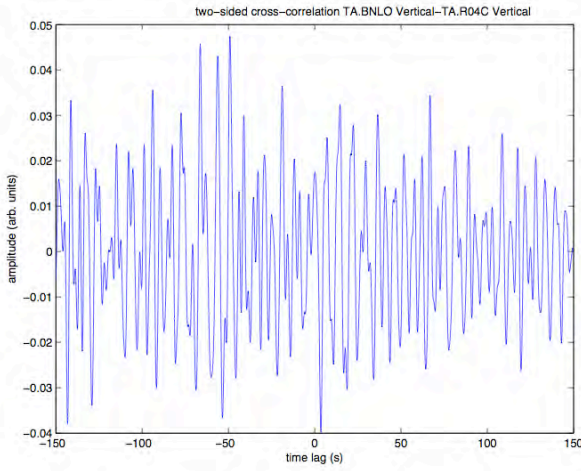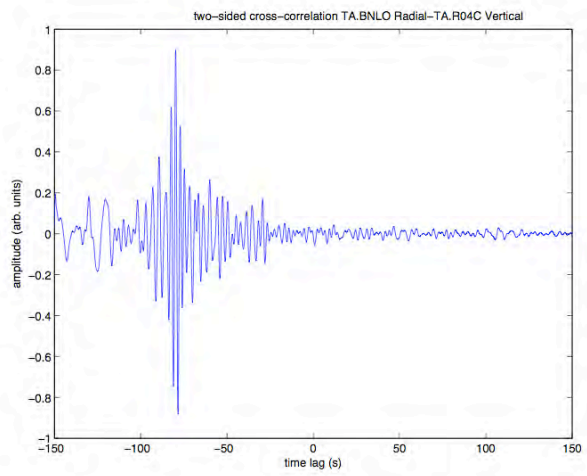
a)   b)

Figure 5. Comparison of (a) vertical-vertical correlation and (b) vertical-radial correlation for stations BNLO and R04C.

15
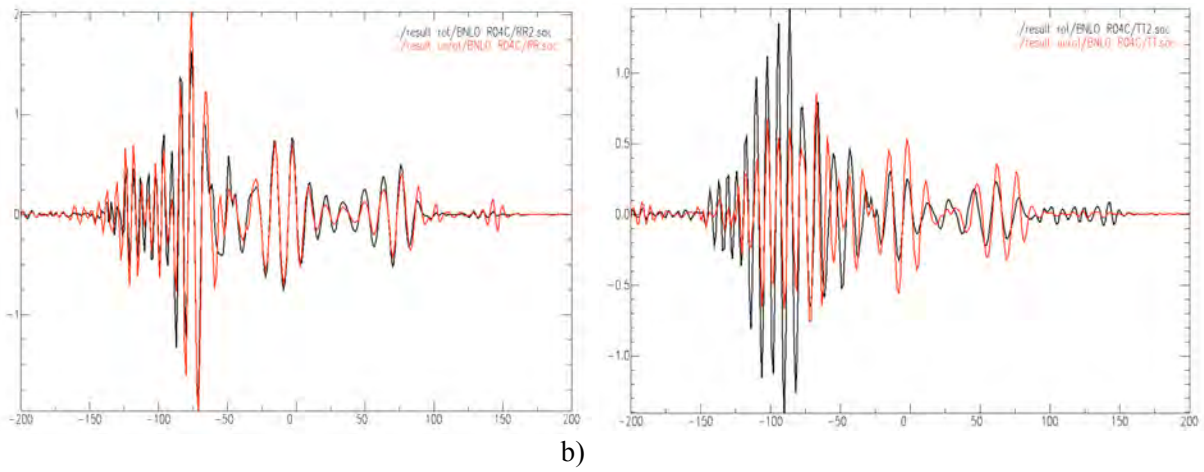
Figure 6. Comparison of Green's function extraction for (a) radial-radial and (b) transverse-transverse components using the process then rotate approach in red versus rotate then process in black.
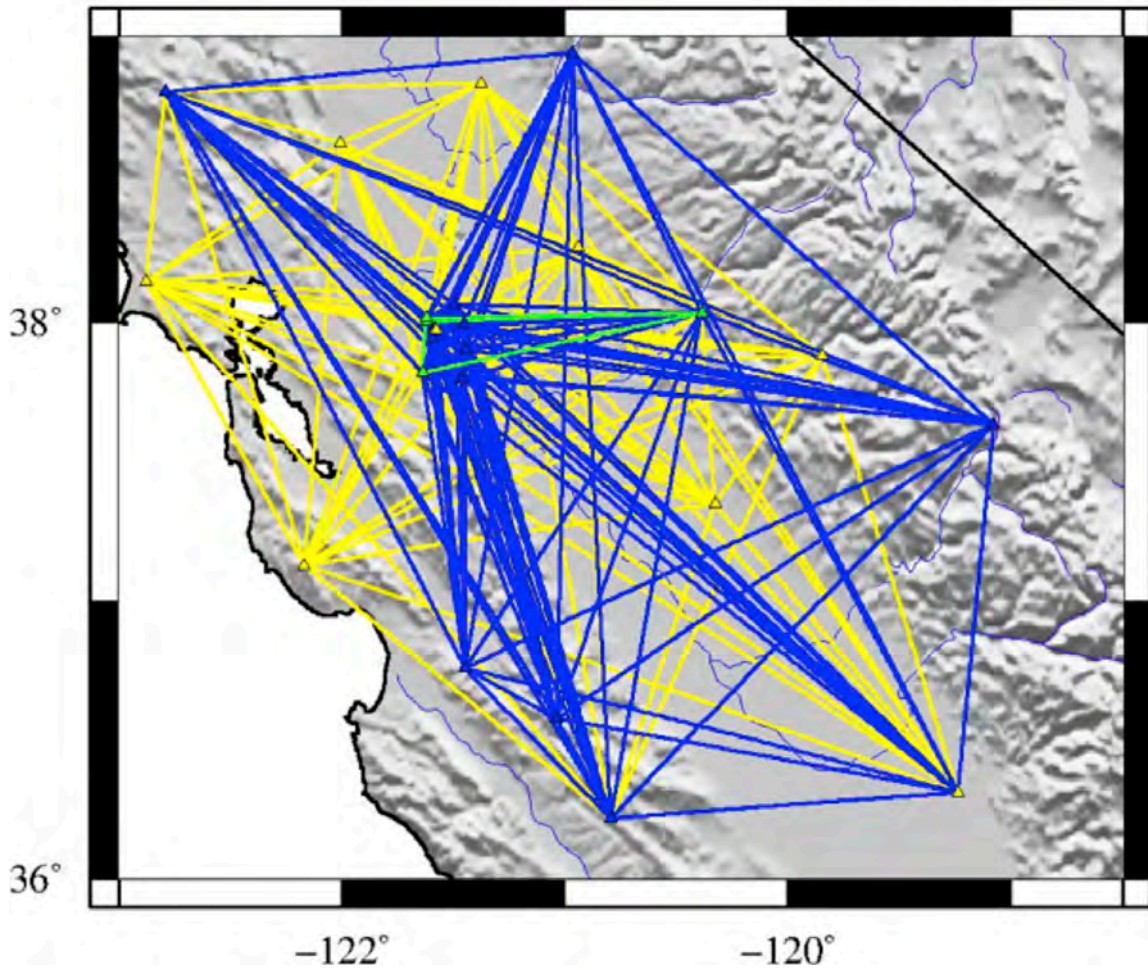
Figure 7. Map showing the paths of the station-pair cross-correlations. Colored lines represent the paths of cross-correlations in 2007 (yellow), 2009 (blue), and both time periods (green).
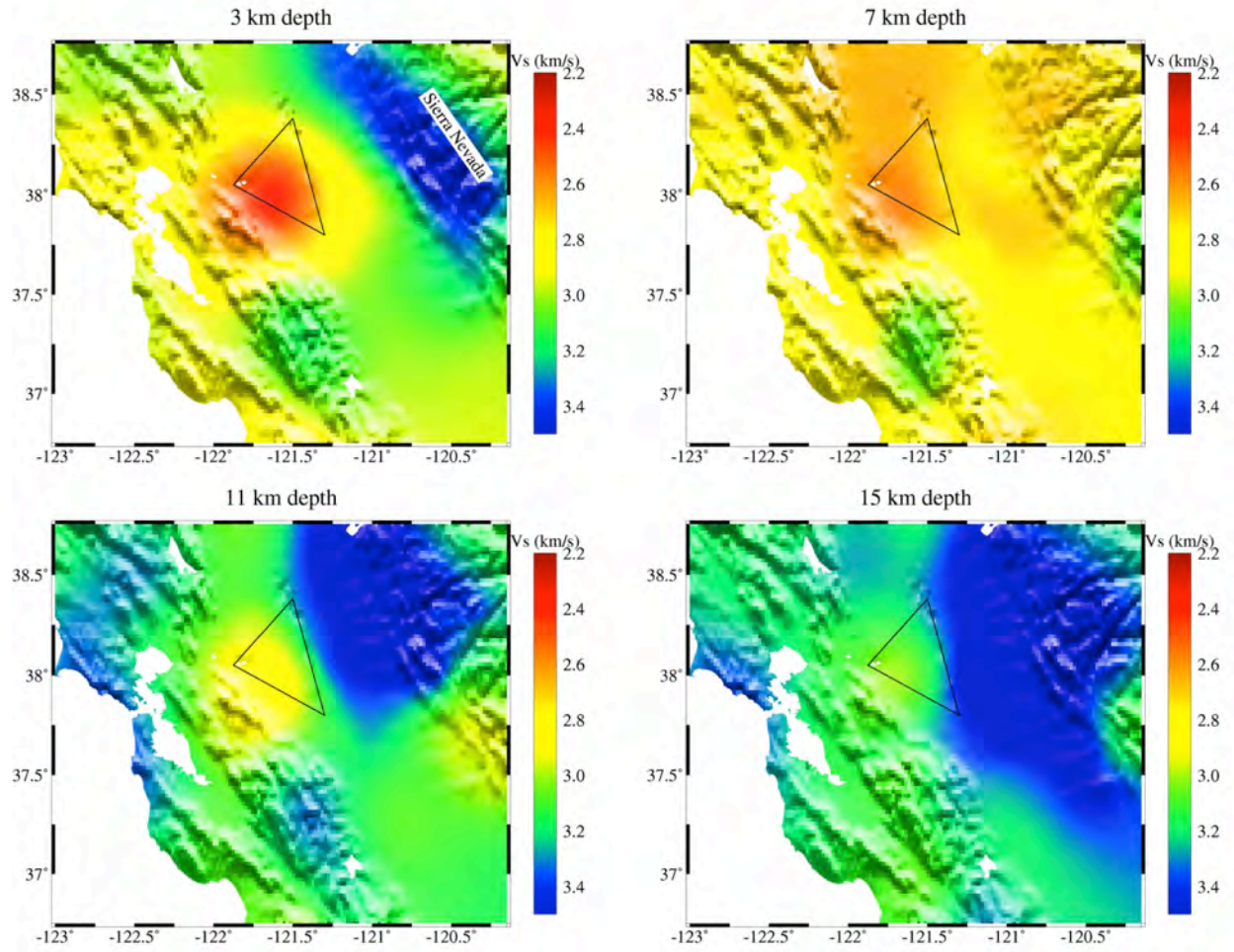
Figure 8. Vs maps for the model from ambient noise tomography, at depths of 3, 7, 11, and 15 km. The color scale is in km/s. The black triangle shows the approximate location of the SSJRD.
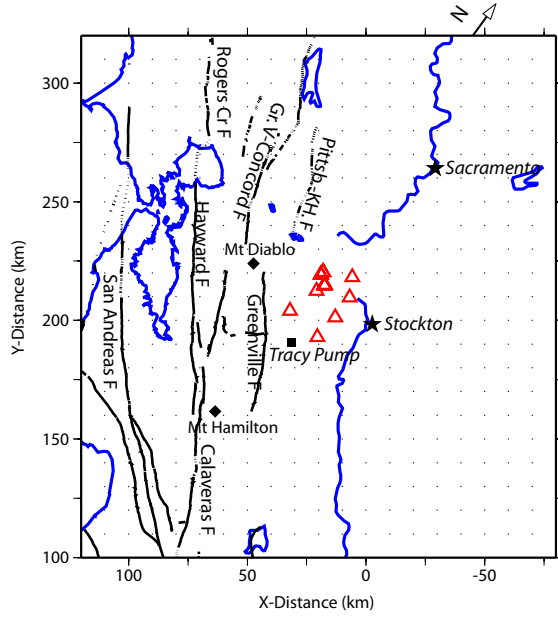
Figure 9. Plot of Q inversion grid area with faults, Delta array, and nearby cities indicated. Red triangles indicate the SSJRD array of Fletcher and Boatwright (2013). The river water exits both through the San Francisco Bay and through the Tracy Pump to southern California.
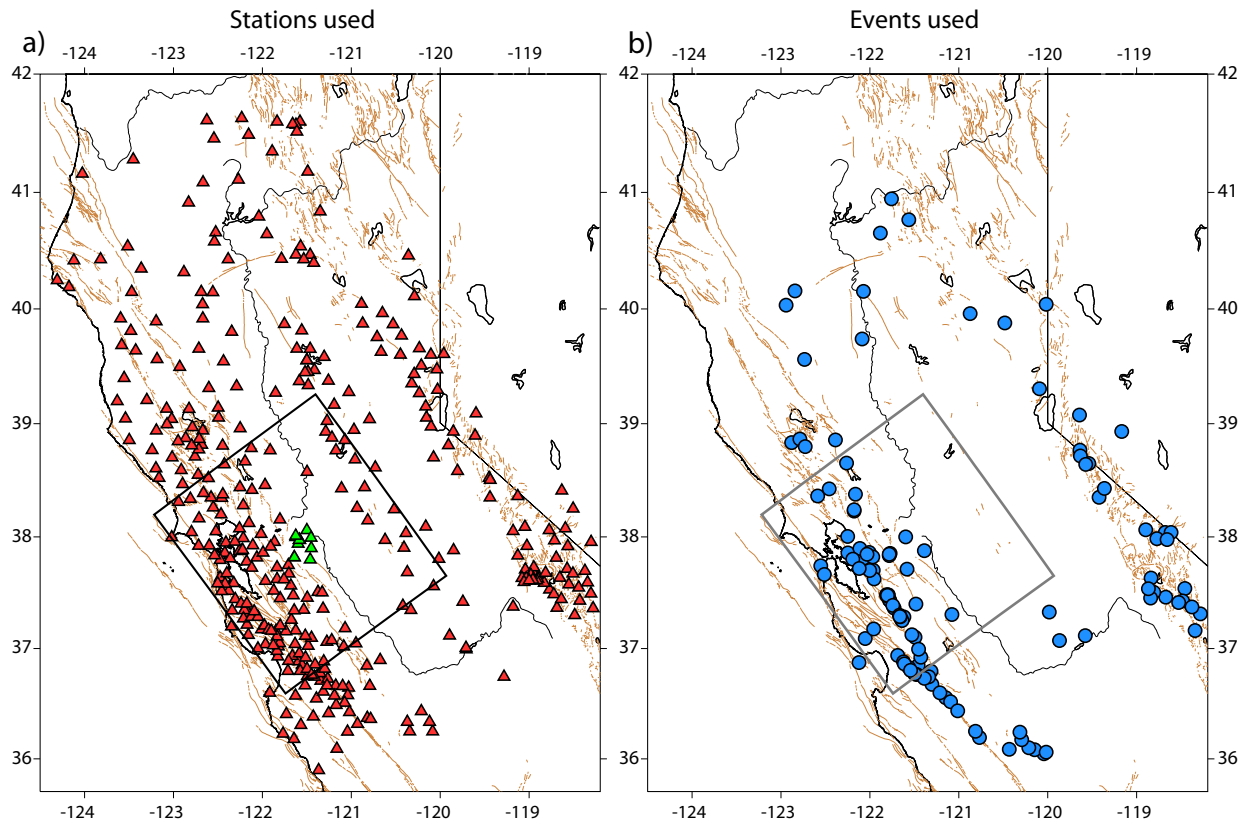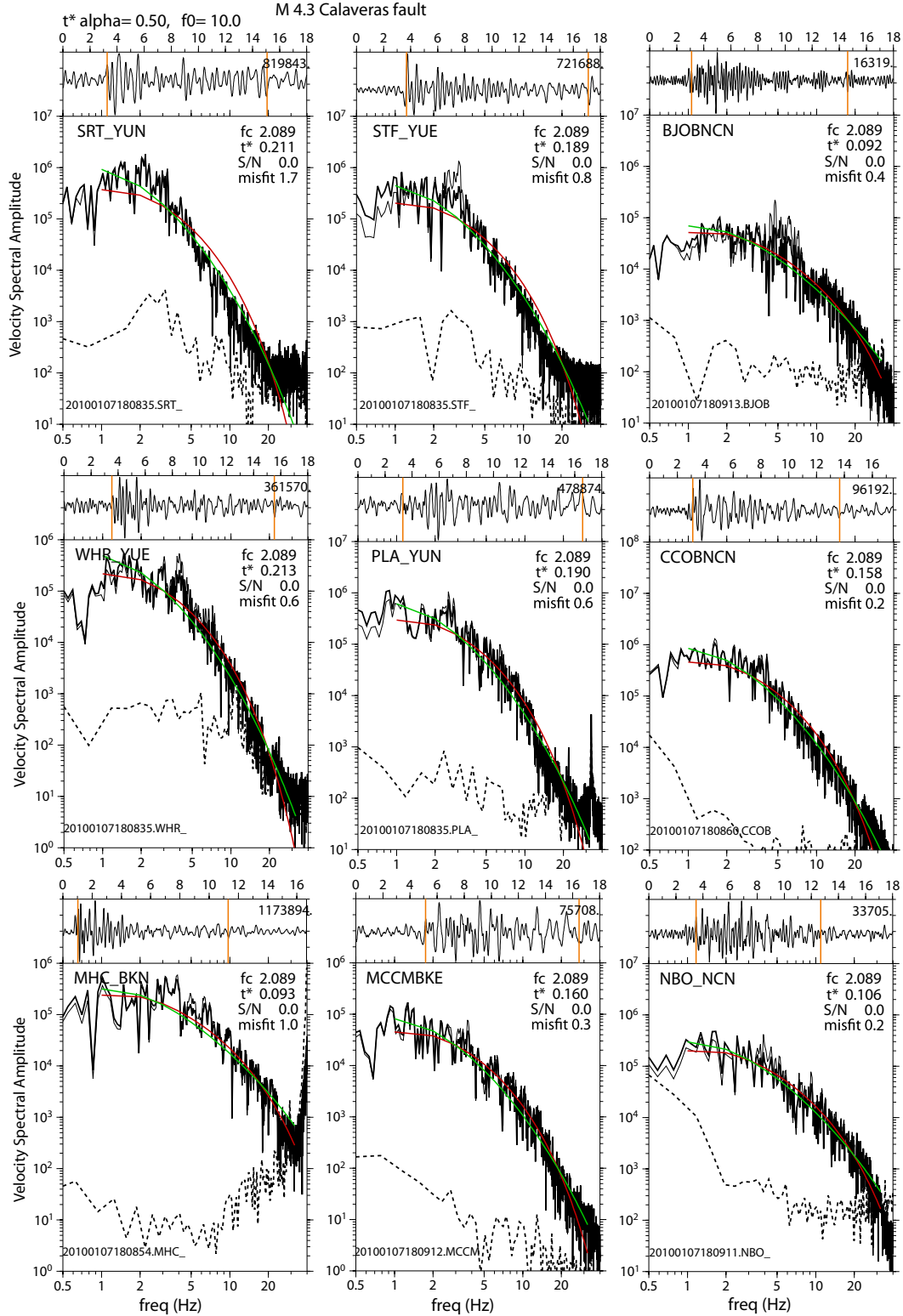

Figure 10. a) Stations used for t* data, green are the Delta array. b) Earthquakes used for t*. Gray box is study area.

Figure 11. An example of t* fitting for the energy-integral S, comparing the frequency independent (red line) and α=0.5 frequency dependent (green line), for a magnitude 4.3 earthquake. The thin line shows the initial spectra, the thick line shows the spectra after removal of site response.
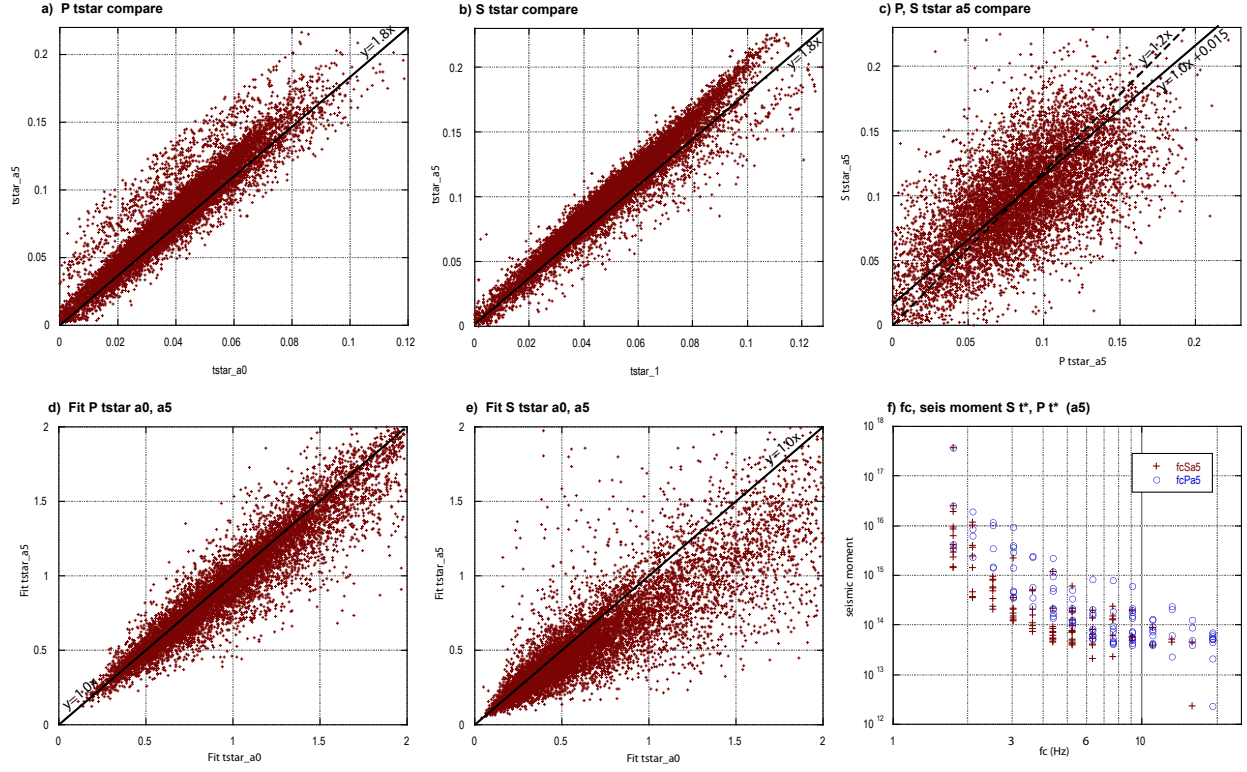
19

Figure 12. Comparison of fitting P and S t* from frequency independent ($\alpha0$: $\alpha = 0$) and frequency dependent ($\alpha5$: $\alpha = 0.5$) solutions. a) P t* for $\alpha0$ compared to $\alpha5$, line shows y = 1.8 x. b) S t* for $\alpha0$ compared to $\alpha5$, line shows y = 1.8 x. c) P t* compared S t*, $\alpha5$, lines show y = 1.0 x + 0.015 and y = 1.2 x (dashed). d) Compare fit for P t* $\alpha0$ versus $\alpha5$. e) Compare fit for S t* $\alpha0$ versus $\alpha5$. f) Compare seismic moment and fc obtained during fitting t* for P and S, $\alpha5$.

a) Z= 4 Vs CA2010

b) Z= 20 Vs CA2010

c) Z= 4 Qs Initial Reg Mod

d) Z= 20 Qs Initial Reg Mod

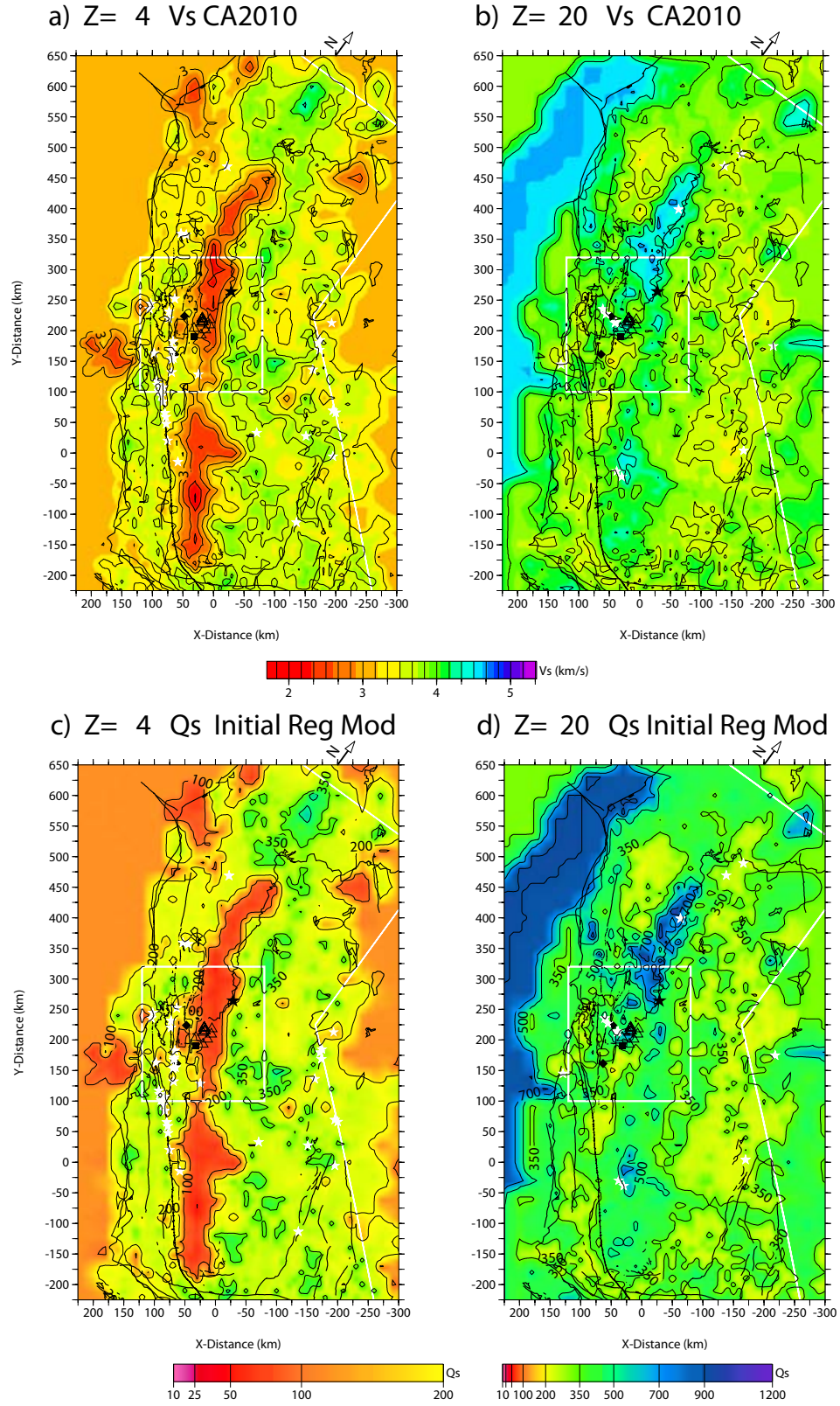Figure 5. Regional California velocity model from Lin et al. (2010), shown at a) 4-km and b)
Figure 13. Regional California velocity model from Lin et al. (2010), shown at a) 4 km and b) 20 km
20-km depth. Initial Qs model obtained by solving for Qs(Vs), shown at c) 4-km and d) 20-km.
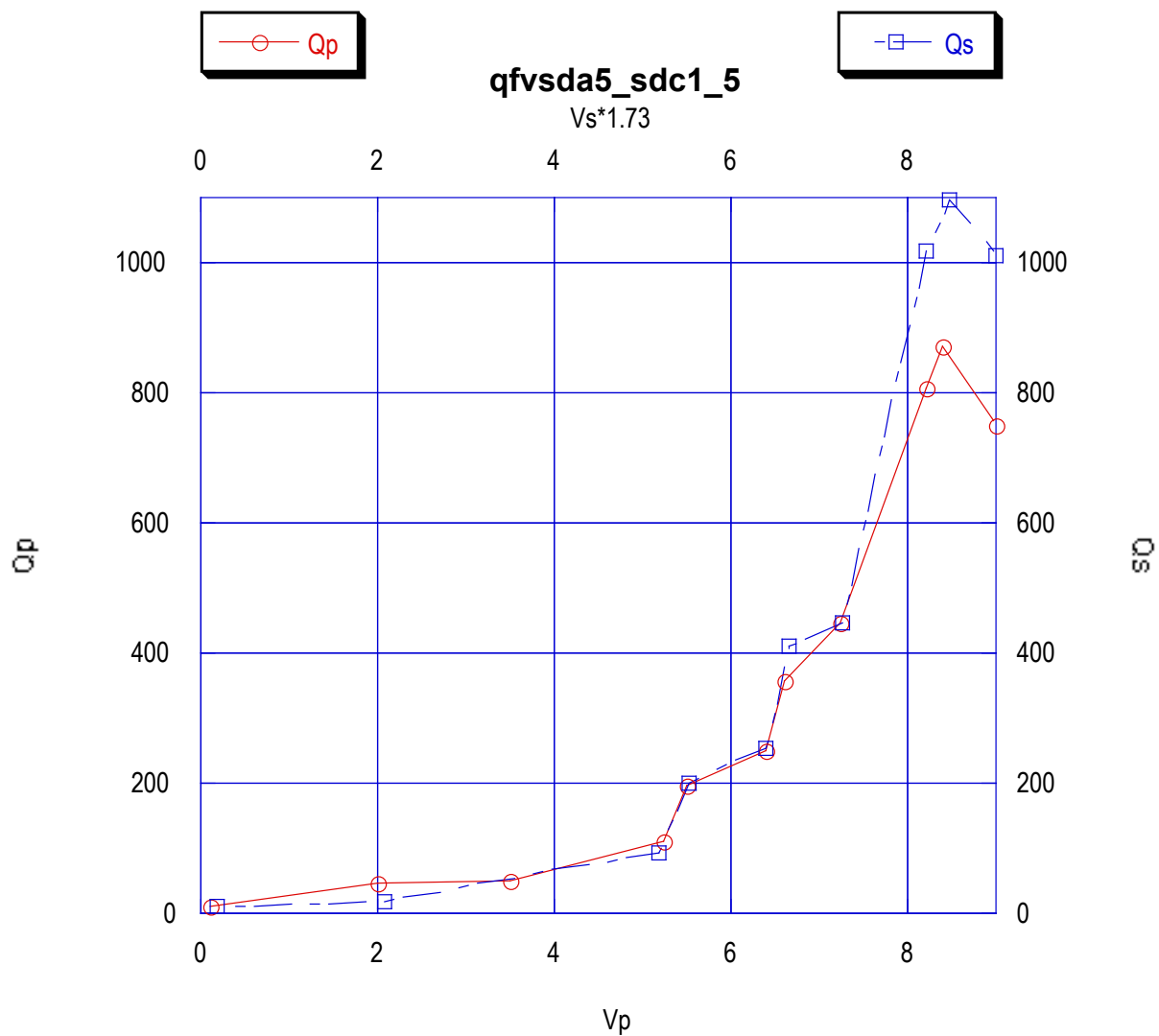depth. Initial Qs model obtained by solving for Qs(Vs), shown at c) 4 km and d) 20 km.

21

Figure 14. Northern California initial Q model was obtained by inverting for Qp as a function of Vp (solid red line) and Qs as a function of Vs (blue dashed line).
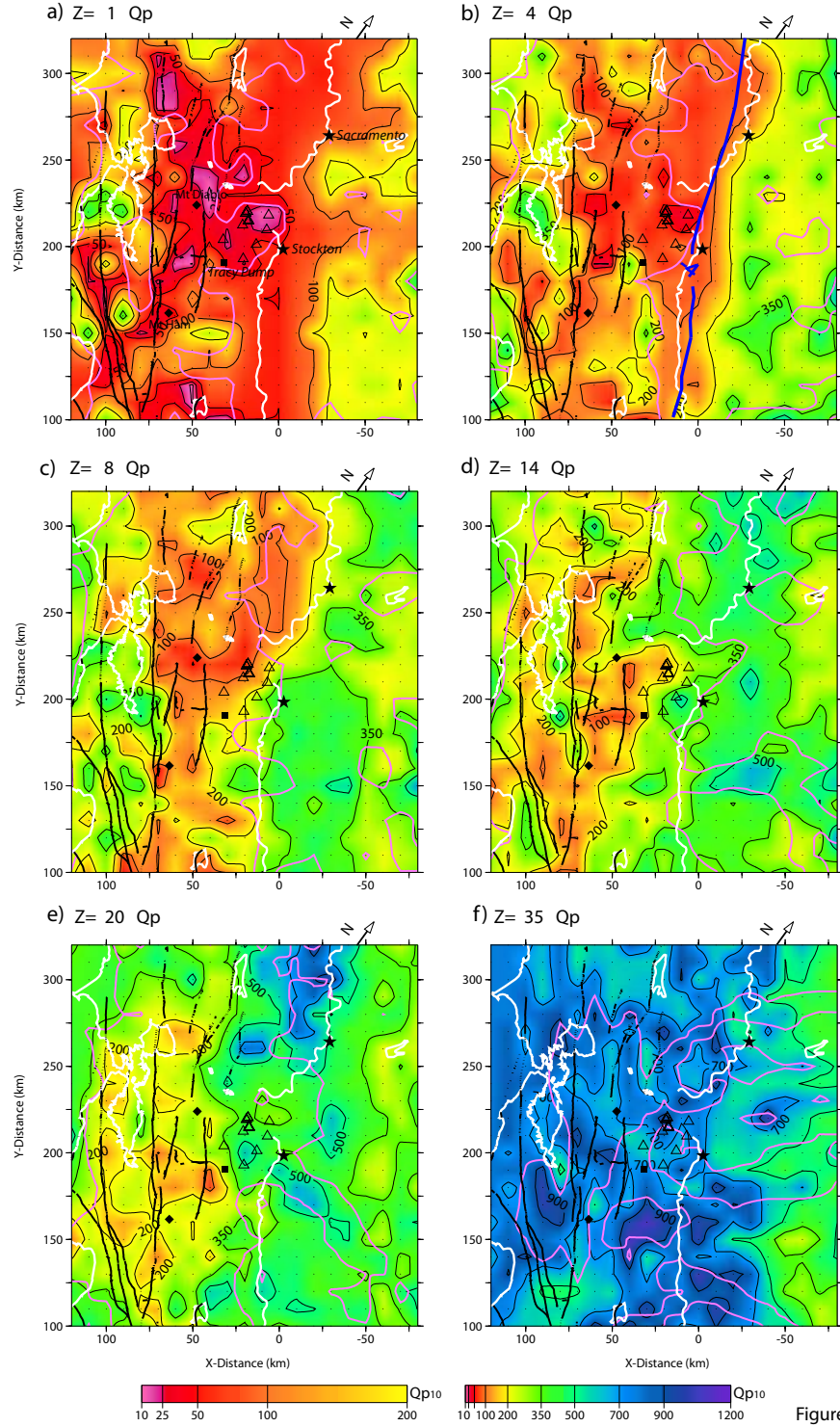
Figure 15. Results for 3D Qp in the Delta region (box in Figures 10 and 13), showing the 3D Qp 10 km grid model at selected depths: a) 1, b) 4, c) 8, d) 14, e) 20, and f) 35 km depth. White lines shows coast and rivers, black lines show faults, towns and features are labeled in (a). Magenta lines indicate the region of adequate resolution from the SF= 3.5 (SF shown in Figure 17). In (b), blue line shows 4 km depth basement contour from Wentworth et al. (1995).
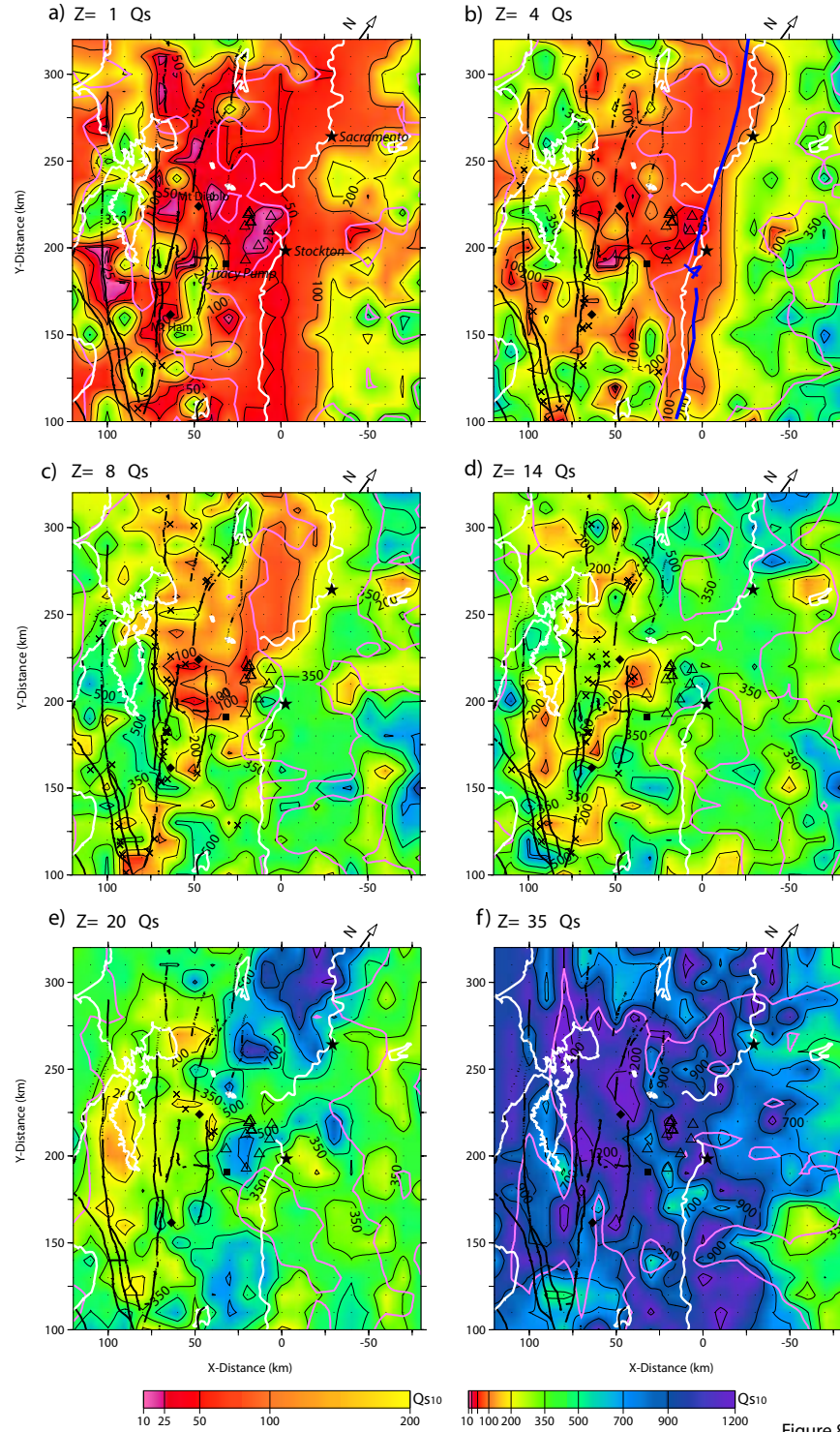
<u>Figure 16.</u> Results for 3D Qs in the Delta region (box in Figures 10 and 13), showing the 3D Qp 10 km grid model at selected depths: a) 1, b) 4, c) 8, d) 14, e) 20, and f) 35 km depth. White lines shows coast and rivers, black lines show faults, towns and features are labeled in (a). Magenta lines indicate the region of adequate data from the SF= 3.5 (SF shown in Figure 17). In (b), blue line shows 4 km depth basement contour from Wentworth et al. (1995).

24
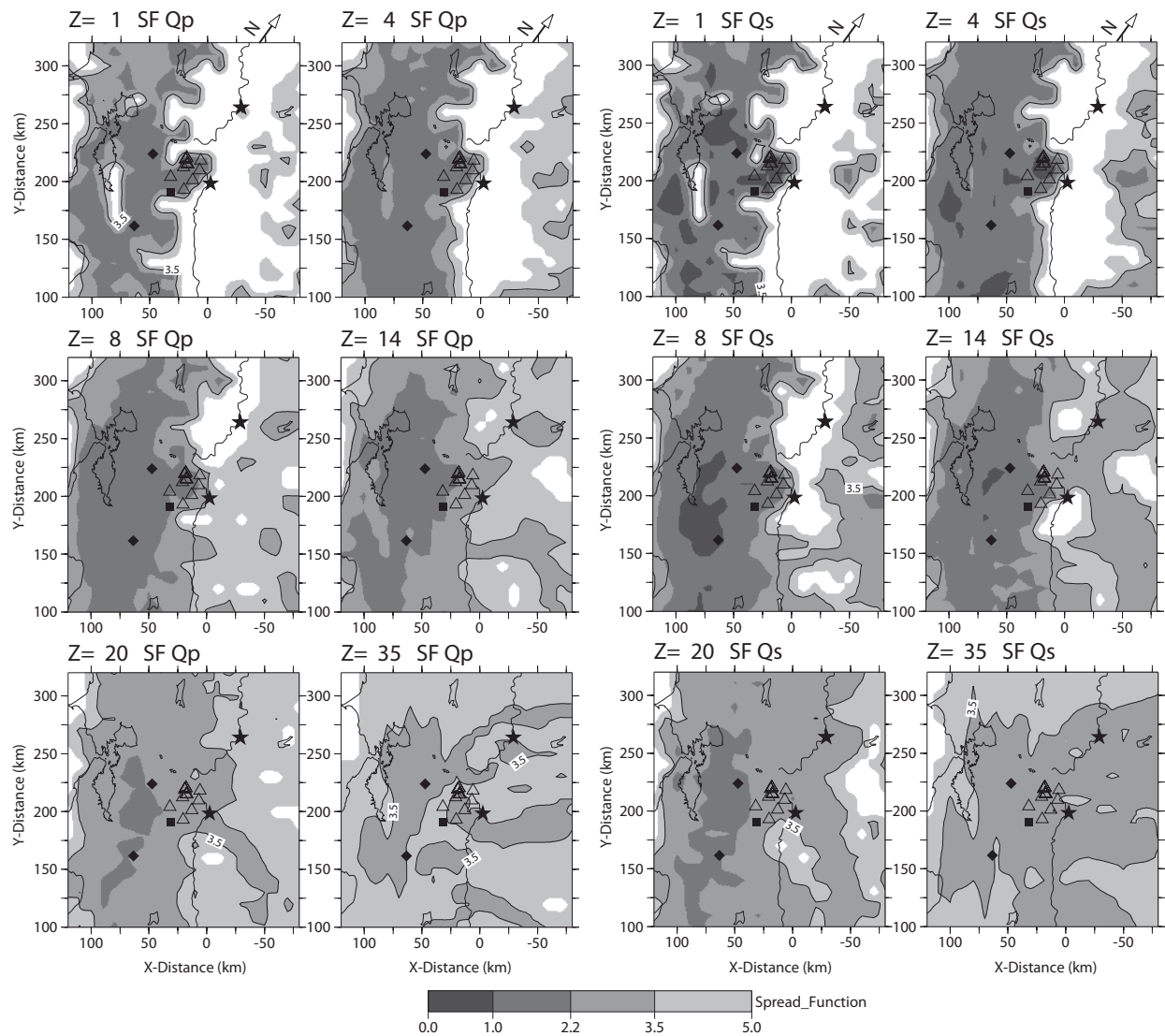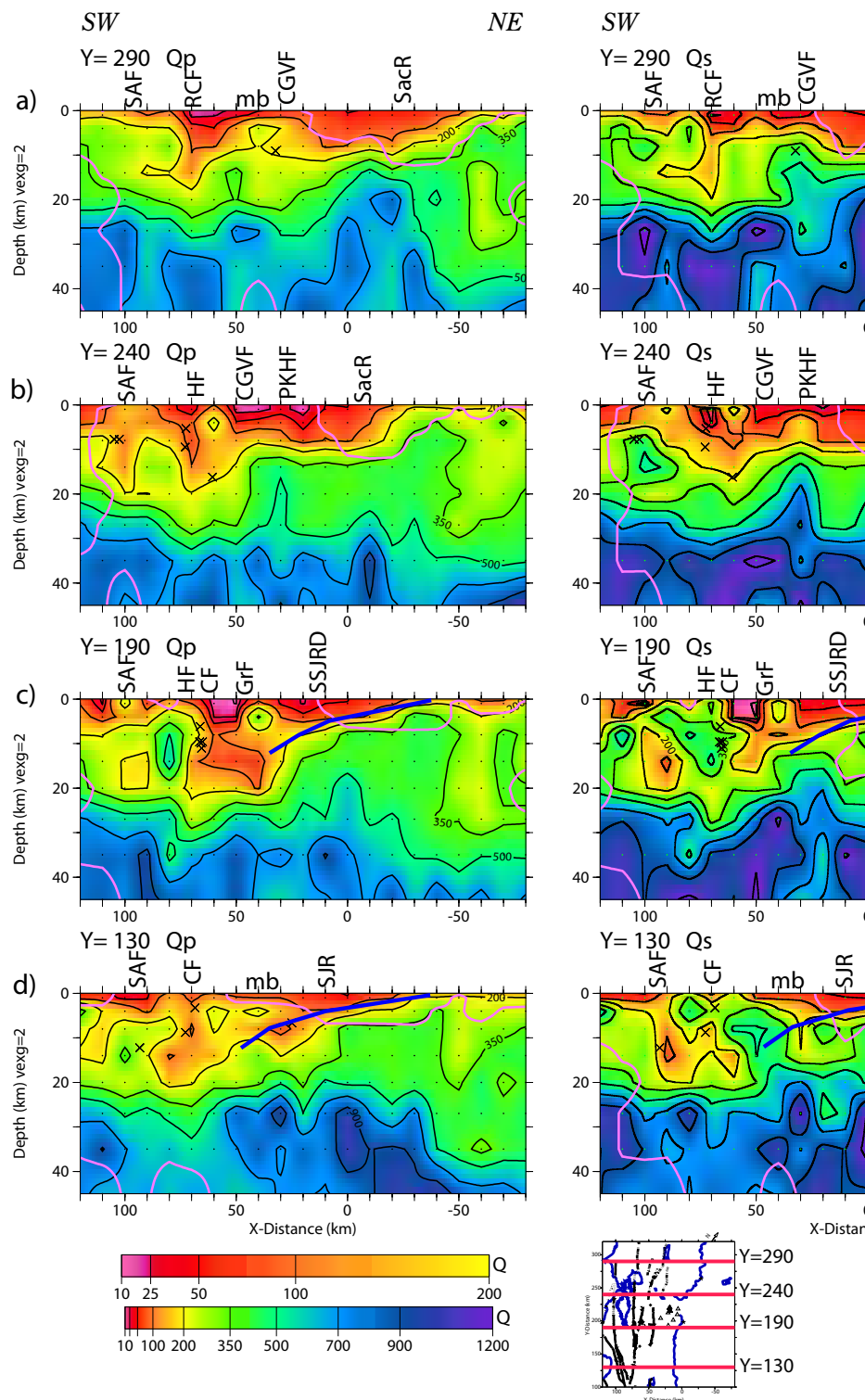
Figure 17. Plots of resolution as indicated by spread function for 3D Qp and Qs for same depths as shown in Figures 15-16.

Figure 18. Cross-sections of the 3D Qp and Qs model for sections indicated in map inset. Vertical exaggeration is 2:1 and faults are labeled. The blue line in c-d is the basement surface from Wentworth et al. (1995). Faults: SAF=San Andreas, RCF=Rogers Creek, CGVF=Concord-Green Valley, HF=Hayward, PKHF=Pittsburgh-Kirby Hills, CF=Calaveras. SacR=Sacramento River, SJR=San Joaquin River, mb=magnetic body.
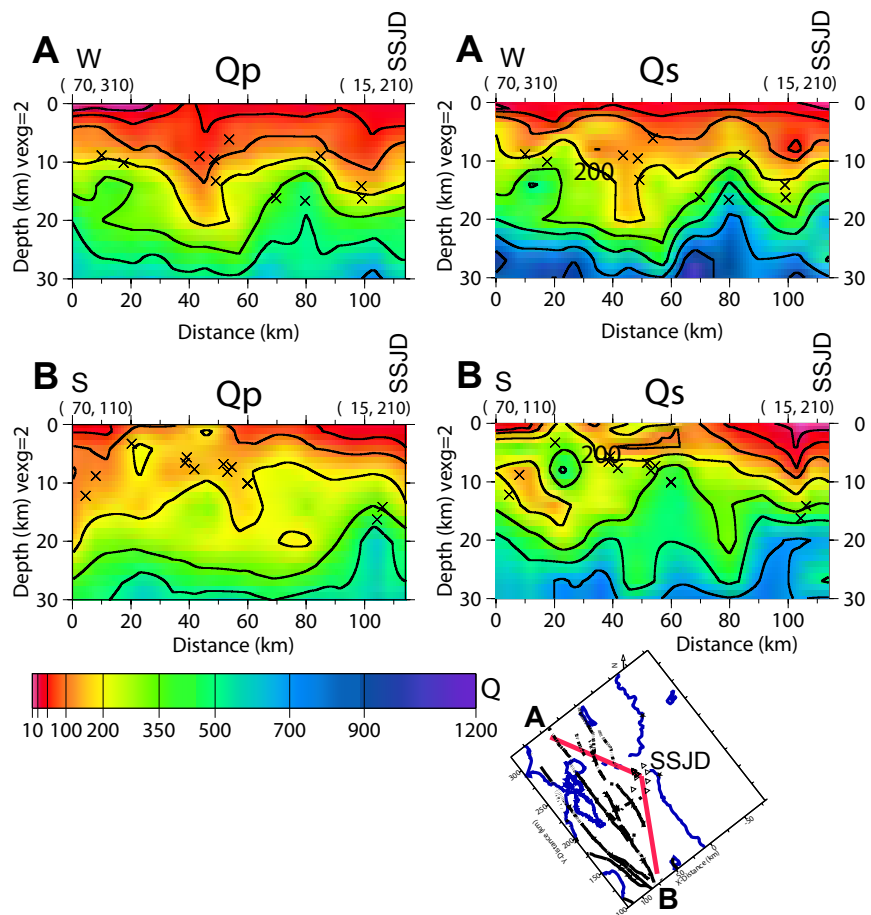
26

Figure 19. Cross-sections of the 3D Qp and Qs model for profiles A, B indicated in map inset. Vertical exaggeration is 2:1.

Problems encountered

Our research effort depended critically on the temporary deployment of the USGS instruments at a larger number of sites in the Delta. Through most of the project, there were very few changes in the instrument deployment in the Delta, limiting our ability to resolve the 3D structure.

Due to spurious signals in the correlated waveforms near time zero for correlations of vertical components, caused by persistent anisotropic noise sources, we switched to correlating vertical and radial waveforms, as suggested by Matt Haney. This strategy produced superior results.

Reports published

Eberhart-Phillips, D., C. Thurber, and J. Fletcher, Imaging P and S attenuation in the Sacramento-San Joaquin Delta region, northern California, *Bull. Seism. Soc. Am.*, submitted.

Teel, A. (2012), Seismic tomography of the Sacramento-San Joaquin River Delta: Joint P-wave/gravity and ambient noise methods, Ph.D. thesis, University of Wisconsin-Madison.

Funding expended for the project

Expenditures as of December 31, 2013 are $160,000.00.

References

Aagaard, B. T., Graves, R. W., Rodgers, A., Brocher, T. M., Simpson, R. W., Dreger, D., Petersson, N. A., Larsen, S. C., Ma, S., and Jachens, R. C. (2010). Ground motion modeling of Hayward fault scenario earthquakes, Part II: Simulation of long-period and broadband ground motions. Bull. Seism. Soc. Am. 100, 2945-2977, doi: 10.1785/0120090379.

Abercrombie, R. (1995). Earthquake source scaling relationships from -1 to 5 ML using seismograms recorded at 2.5-km depth. J. Geophys. Res 100, 24,015-24,036.

Asano, Y., and Hasegawa, A. (2004). Imaging the fault zones of the 2000 western Tottori earthquake by a new inversion method to estimate three-dimensional distribution of the scattering coefficient. J. Geophys. Res 109, B06306,doi:10.1029/2003JB002761.

Birch, F. (1961). The velocity of compressional waves in rocks to 10 kilobars, Part 2. J. Geophys. Res. 66, 7.

Blake, M. C., Jayko, A. S., McLaughlin, R. J., and Underwood, M. B. (1988). Metamorphic and tectonic evolution of the Franciscan Complex, northern California. In "Metamorphism and crustal evolution of the Western United States, Rubey Vol. 7." (W. G. Ernst, Ed.), pp. 1035-1060. Prentice-Hall, Englewood Cliffs, N. J.

Blakely, R. J. (1995). Potential theory in gravity and magnetic applications, Cambridge University Press, ISBN: 0-521-41508-X.

Boatwright, J., Bundock, H., Luetgert, J., Seekins, L., Gee, L., and Lombard, P. (2003). The dependence of PGA and PGV on distance and magnitude inferred from northern California ShakeMap data. Bull. Seism. Soc. Am. 93, 2043-2055.

Boatwright, J., Choy, G. L., and Seekins, L. (2002). Regional estimates of radiated energy. Bull. Seism. Soc. Am. 92, 1241-1255.

Boatwright, J., and Seekins, L. (2011). Regional spectral analysis of three moderate earthquakes in northeastern North America. Bull. Seism. Soc. Am. 101, 1769-1782.

Boore, D. M. (2003). Simulation of ground motion using the stochastic method. Pure and Applied Geophyics 160, 635-676.

Brocher, T. M. (2005). Empirical relations between elastic wavespeeds and density in the earth's crust, Bull. Seis. Soc. Am. 95, 2081-2092.

Brocher, T. M. (2008). Compressional and shear-wave velocity versus depth relations for common rock types in northern California. Bull. Seism. Soc. Am. 98, 950-968.

Christensen, N. I., and Mooney, W. D. (1995). Seismic velocity structure and composition of the continental crust: A global view. J. Geophys. Res. 100, B7, 9761-9788.

Eberhart-Phillips, D., and Chadwick, M. (2002). Three-dimensional attenuation model of the shallow Hikurangi subduction zone in the Raukumara Peninsula, New Zealand. J. Geophys. Res. 107, doi:10.1029/2000JB000046.

Eberhart-Phillips, D., McVerry, G., and Reyners, M. (2010). Influence of the three-dimensional distribution of Q and crustal structure on ground motions from the Mw 7.2 2003 Fiordland, New Zealand, earthquake. Bull. Seism. Soc. Am. 100, 1225-1240.

Eberhart-Phillips, D., and Reyners, M. (2012). Imaging the Hikurangi plate interface region with improved local-earthquake tomography. Geophys. J. Int. 190, 1221-1242, doi: 10.1111/j.1365-246X.2012.05553.x.

Fletcher, J. B., and Boatwright, J. (2013). Site response and basin waves in the Sacramento-San Joaquin Delta, California. Bull. Seism. Soc. Am. 103, 196-210.

Forte, A. M., Woodward, R. L., and Dziewonski, A. M. (1994). Joint inversion of seismic and geodeynamic data for models of three-dimensional mantle heterogeneity. J. Geophys. Res. 99, 21,857-21,877.

Frankel, A. (1991). Mechanisms of seismic attenuation in the crust: scattering and anelasticity in New York state, South Africa, and southern California. J. Geophys. Res. 96, 6269-6289.

Frasseto, A. M., Zandt, G., Gilbert, H., Owens, T. J., and Jones, C. H. (2011). Structure of the Sierra Nevada from receiver functions and implications for lithospheric foundering. Geosphere 7, 898-921.

Gardner G. H. F., Gardner, L. W., Gregory, A. R. (1974). Formation velocity and density – the diagnostic basics for stratigraphic traps, Geophysics 39, 6, 770-780.

Godfrey, N., Beaudoin, B. C., Klemperer, S. L., and Mendocino Working Group (1997). Ophiolitic basement to the Great Valley forearc basin, northern California, from seismic and gravity data: Implications for crustal growth at the North American continental margin. Geol. Soc. Am. Bull. 109, 1536-1562.

Godfrey, N. J., and Klemperer, S. L. (1998). Ophiolitic basement to a forearc basin and implications for continental growth: the Coast Range/Great Valley ophiolite, California. Tectonics 17, 558-570.

Hardebeck, J. L., Michael, A. J., and Brocher, T. M. (2007). Seismic velocity structure and seismotectonics of the eastern San Francisco Bay region, California. Bull. Seism. Soc. Am. 97, 826-842, doi 10.1785/0120060032.

Hartzell, S, Leeds, A., Frankel, and Michael, A. J. (1996). Site response for urban Los Angeles using aftershocks of the Northridge earthquake. Bull. Seis. Soc. Am. 86, 168-192.

Holbrook, W. S., Brocher, T. M., ten Brink, U. S., and Hole, J. A. (1996). Crustal structure of a transform plate boundary: San Francisco Bay and the central California continental margin. J. Geophys. Res 101, 22,311-22,334.

Hole, J. A., T. M. Brocher, S. L. Klemperer, T. Parsons, H. M. Benz, and Furlong, K. P. (2000). Three-dimensional seismic velocity structure of the San Francisco Bay area. J. Geophys. Res 105, 13,859-13,874.

Jachens, R. C., Griscom, A., and Roberts, C. W. (1995). Regional extent of Great Valley basement west of the Great Valley, California: Implications for extensive tectonic wedging in the California Coast Ranges. J. Geophys. Res 100, 12,769-12,790.

Jackson, I., Fitzgerald, J. D., Faul, U. H., and Tan, B. H. (2002). Grain-size-sensitive seismic wave attenuation in polycrystalline olivine. J. Geophys. Res. 107, ECV5 doi:1029/2001JB001225.

Kenner, S. J., and Segall, P. (2003). Lower crustal structure in northern California: implications from strain rate variations following the 1906 San Francisco earthquake. J. Geophys. Res 108, doi:10.1029/2001JB000189003.

Koulakov, I., Bindi, D., Parolai, S., Grosser, H., and Milkereit, C. (2010). Distribution of seismic velocities and attenuation in the crust beneath the North Anatolian Fault (Turkey) from local earthquake tomography. Bull. Seism. Soc. Am. 100, 207-224.

Lees, J. M., VanDecar, J. C. (1991). Seismic tomography constrained by Bouguer gravity anomalies: Applications in Western Washington. PAGEOPH 135, 1, 31-52.

Lin, G., C. H. Thurber, H. Zhang, E. Hauksson, P. M. Shearer, F. Waldhauser, T. M. Brocher, and J., and Hardebeck. (2010). A California statewide three-dimensional seismic velocity model from both absolute and differential times. Bull. Seism. Soc. Am. 100, 225-240; DOI: 10.1785/0120090028.

Lines, L.R., Schultz, A. K., and Treitel, S. (1988). Cooperative inversion of geophysical data. Geophysics 53, 8-20.

Lund, J., Hanak, E., Fleenor, W., Howitt, R., Mount, J., and Moyle, P. (2007). Envisioning Futures for the Sacramento-San Joaquin Delta, pp. 325. Public Safety Policy Institute of California.

Madariaga, R. (1976). Dynamics of an expanding circular fault. Bull. Seism. Soc. Am. 66, 639-666.

Malagnini, L., Mayeda, K., Uhrhammer, R., Akinci, A., and Herrmann, R. B. (2007). A regional ground motion excitation/attenuation model for the San Francisco region. Bull. Seism. Soc. Am. 97, 843-862.

Masterlark, T., M. Haney, H. Dickinson, T. Fournier, and C. Searcy (2010). Rheologic and structural controls on the deformation of Okmok volcano, Alaska: FEMs, InSAR, and ambient noise tomography, J. Geophys. Res., 115, B02409, doi:10.1029/2009JB006324.

Michelini, A. (1991). "Fault zone structure determined through the analysis of earthquake arrival times." Unpublished Ph. D. thesis, Univ. Calif., Berkeley.

Moores, E. M., Wakabayashi, J., and Unruh, J. R. (2002). Crustal-scale cross-section of the U.S. Cordillera, California and beyond, its tectonic significance, and speculations on the Andean orogeny. Int. Geology Rev. 44, 479-500.

Morelli, C., C. Gantar, R. K. McConnell, B. Szabo, and U. Uotila (1971). The International Gravity Standardization Net 1971, IUGG IAG Special Publication No. 4, 194 pp.

Nielsen, L., and Jacobsen, B. H. (2000). Integrated gravity and wide-angle seismic inversion for two-dimensional crustal modeling. Geophys. J. Int. 140, 222-232.

Olsen, K. B. (2000). Site amplification in the Los Angeles Basin from three-dimensional modeling of ground motion. Bull. Seis. Soc. Am. 90, 77-94.

Parsons, T., Blakely, R. J., and Brocher, T. M. (2001). A simple algorithm for sequentially incorporating gravity observations in seismic traveltime tomography. Int. Geol. Rev., 43, 1073-1086.

Platt, J. P., and Behr, W. M. (2011). Grainsize evolution in ductile shear zones: Implications for strain localization and the strength of the lithosphere. J. Structural Geol. 33, 537-550.

Raoof, M., Herrmann, R. B., and Malagnini, L. (1999). Attenuation and excitation of three-component ground motion in southern California. Bull. Seism. Soc. Am. 89, 888-902.

Reyners, M., Eberhart-Phillips, D., and Martin, S. (2013). Prolonged Canterbury earthquake sequence linked to widespread weakening of strong crust. Nature Geoscience in press.

Rietbrock, A. (2001). P-wave attenuation structure in the fault area of the 1995 Kobe earthquake. J. Geophys. Res. 106, 4141-4154.

Roecker, S., Thurber, C., and McPhee, D. (2004). Joint inversion of gravity and arrival time data from Parkfield: new constraints on structure and hypocenter locations near the SAFORD drill site. Geophys. Res. Lett. 31, L12S04, doi:10.1029/2003GL019396.

Roy, L., Sen, M. K., McIntosh, K., Stoffa, P. L., and Nakamura, Y. (2005). Joint inversion of first arrival seismic travel-time and gravity data. J. Geophys. Eng. 2, 277-289.

Savino, J. M., Rodi, W. L., Goff, R. C., Jordan, T. H., Alexander, J. H., and Lambert, D. G. (1977). Inversion of combined greophysical data for determination of structure beneath the Imperial Valley geothermal region. U.S. DOE, Systems, Science and Software, Final Tech. Rep. SSS-R-78-3412.

Semblat, J. F., Dangla, P., and Kham, M. (2002). Seismic site effects for shallow and deep alluvial basins: in-depth motion and focusing effects. Soil Dyn. Earth. Eng. 22, 849-854.

Talwani, M. (1973). Computer usage in the computation of gravity anomalies, Methods Comput. Phys., 13, 343-389.

Teel, A. C. (2012). "Seismic Tomography of the Sacramento - San Joaquin River Delta: Joint P-wave/Gravity and Ambient Noise Methods." Unpublished Ph.D. thesis, Univ. Wisconsin-Madison.

Thurber, C., Brocher, T. M., Zhang, H., and Langenheim, V. (2007). Three-dimensional P-wave velocity model for the San Francisco Bay region. J. Geophys. Res 112, B07313, doi:10.1029/2006JB004682.

Thurber, C., Zhang, H., Brocher, T. M., and Langenheim, V. (2009). Regional three-dimensional seismic velocity model of the crust and uppermost mantle of northern California. J. Geophys. Res 114, B01304, doi:10.1029/2008JB005766.

URS Corporation, and J.R.Benjamin & Associates. (2009). Delta risk management strategy (DRMS), Phase 6 final report. California Department of Water Resources.

Waldhauser, F. (2009). Near real-time double-difference event location using long-term seismic archives, with application to northern California. Bull. Seism. Soc. Am. 99, 2736-2748.

Wang, Y.-J., Ma, K.-F., Mouthereau, F., and Eberhart-Phillips, D. (2009). Three dimensional Qp- and Qs-Tomography beneath Taiwan Orogenic Belt: Implications for Tectonic and Thermal Structure. Geophys. J . Int., doi: 10.1111/j.1365-246X.2009.04459.x.

Wentworth, C. M., Fisher, G. R., Levine, P., and Jachens, R. C. (1995). The surface of crystalline basement, Great Valley and Sierra Nevada, California: A digital map database.

Wentworth, C. M., and Zoback, M. D. (1989). The style of late Cenozoic deformation at the eastern front of the California Coast Ranges. Tectonics 8, 237-246.

Winkler, K. W., and Murphy III, W. F. (1995). Acoustic velocity and attenuation in porous rocks. In "Rock physics and phase relations: A handbook of physical constants." (T. J. Ahrens, Ed.), pp. 20-34. AGU, Washington DC.

Zhang, H., and C. Thurber (2006). Development and applications of double-difference tomography, Pure App. Geophys., 163, 373-403, doi:10.1007/s00024-005-0021-y.